Extension of plasticity theory to debonding, grain dissolution and chemical damage of calcarenites

Matteo Oryem Ciantia[1] & Claudio di Prisco[2]

[1] *Departamiento de Ingeniería del Terreno, UPC, Barcelona, Spain, -* matteo.ciantia@upc.edu

[2]*Politecnico di Milano, Piazza L. da Vinci 32, 20133, Milano, Italia -* claudio.diprisco@polimi.it

ABSTRACT

The mechanical properties of calcarenites are known to be significantly affected by water saturation: both stiffness and strength decrease for wetting in the short term and for chemical dissolution in the long term. Both processes mainly affect bonds among grains: immediately after inundation depositional bonds fall in suspension whereas diagenetic bonds dissolve more slowly. In this paper, the authors started from the micro-structural analysis of the weathering processes to conceive a strain hardening hydro – chemo - mechanical coupled elasto-plastic constitutive model. The concept of extended hardening rules is here enriched: weathering functions have been determined by employing a micro to macro simple upscaling procedure. Chemical damage is incorporated in the formulation by means of a scalar damage function. Its evolution is also described by using a multiscale approach. A new term is added to the strain rate tensor in order to incorporate the dissolution induced chemical deformations developing once the soft rock is turned into a granular material. A calibration procedure for the constitutive parameters is suggested and the model is validated by using both coupled and uncoupled chemo mechanical experimental test results.

KEY WORDS:

Calcarenite; Carbonate rocks; Weathering, Hydro-Chemo-mechanical coupling; inundation; dissolution; short term debonding; long term debonding; chemical deformations

1 Introduction:

This paper focuses on the process of degradation induced in calcareous rocks by water saturation. In particular, an elastoplastic constitutive model, capable of accounting for the non-mechanical processes occurring at the micro-scale when pores are inundated by water will be hereafter presented: this is based on the strain hardening elasto-plastic approach proposed by Nova (1997, 2000) and is derived from a microstructural interpretation of the hydro-chemo-mechanical processes described in Ciantia et al, 2015.

From a macroscopic viewpoint, calcarenites are homogenous highly porous materials, and, at the micro scale, their fabric is characterized by three main components (Folk, 1959): calcareous grains, micrite (microcrystalline calcite mud matrix) and sparite (sparry calcite cement). As was observed by Ciantia et al, 2015, the loose calcite mud, suspended in the pore space of the wet material, forms, in case the material is dried, menisci shaped loose bonds. These, hereafter referred to as depositional bonds, re-suspend once the material is re-inundated with water. On the other hand, the calcite cement, composing the bonds hereafter named diagenetic, seems not to be affected by water in the short term but in the long term is involved in dissolution processes (Ciantia et al, 2015). Therefore, as is schematically suggested by Fig. 1, in general, the weathering debonding taking place in case rocks interact with water can be described as the result of three microscopic elementary mechanisms

i) *the short term debonding* (STD). During saturation water penetrating through the porous structure damages the depositional bonds and the powder composing them falls almost instantaneously into suspension. This induces the marked loss in both strength and stiffness testified by Ciantia et al, 2012, 2013, Castellanza et al 2009a. It was also observed that the STD mechanism evolves for a saturation degree ranging between 0 (dry) and 0.4 (partially

saturated state). The driving variables for the STD process are thus both the degree of saturation, S_r, and the amount of powder entrapped inside the porous matrix, M_P (Ciantia, 2013; Ciantia et al, 2015). Analogously to S_r, M_P is a state variable for the material and its variation, ΔM_P normalized with respect to the initial powder mass M_{P_0} is here defined as

$$\xi_{sus} = \Delta M_P / M_{P_0} \tag{1}$$

ξ_{sus} is constrained by inequality $0 \leq \xi_{sus} \leq 1$. When $\xi_{sus}=1$, the STD process is completed that is, the powder is entirely suspended.

ii) *the long term debonding* (LTD). This is due to the chemical dissolution of diagenetic bonds taking place when calcarenite is flooded by water for a long period of time. With time, these bonds are progressively weathered until the material is transformed into a calcareous soil. The process evolution is governed by both the rate of the dissolution reaction and the ionic composition of the bulk fluid. The driving variable for LTD is the reaction progress variable (De Groot, 1966) defined as the accumulated relative mass removal of calcite from diagenetic bonds and grains over the initial mass:

$$\xi_{dis} = \Delta M / M_0 \tag{2}$$

where ΔM and M_0 are the dissolved and the initial mass, respectively.

Analogously to ξ_{sus}, also ξ_{dis} is constrained by the inequality $0 \leq \xi_{dis} \leq 1$. When $\xi_{dis}=1$, the reaction is completed: that is, calcite is totally dissolved.

iii) *the grain dissolution process* (GDP). This consists in the chemical dissolution of the calcareous grains evolving with LTD and ruled by the same state variable ξ_{dis}.

As is suggested by the experimental evidence (Ciantia, 2013, Ciantia et al, 2015, 2014), the time scales characterizing, on one hand, the STD process and, on the other, the LTD and

the GDP processes are totally different. While the STD process evolves in few seconds, the LTD and GDP, depending on the ionic concentration of the fluid require longer periods of time. For instance, as detailed in Ciantia and Hueckel 2013, to dissolve 5% of calcite in water with a neutral pH for an open system scenario about 1.8 years are needed. Therefore these processes will be assumed to be uncoupled. For this reason, during saturation, the powder mass is assumed to remain constant and hence, ξ_{sus} to exclusively depend on the degree of saturation ($\xi_{sus}=\xi_{sus}(S_r)$). Before entering into the details of the constitutive model, in Fig. 2a, a phase diagram in the $\xi_{dis}-S_r$ plane for calcarenite is proposed and the weathering path is sketched. In Fig. 2b, according to the assumptions above, the corresponding evolution with time of the previously mentioned variables is shown. In particular, during saturation, since the inundation phase is assumed to be rapid enough to prevent any dissolution, only the STD process is assumed to take place, consequently, ξ_{dis} is considered to be constant, while ξ_{sus} evolves from 0 to 1 with the saturation index S_r. As was mentioned above, STD evolves for a limited range of degree of saturation. In particular S_r^* is the minimum degree of saturation necessary for all the depositional bonds to suspend. Once the material is saturated, dissolution is assumed to start and hence both LTD an GDP evolve until a critical value of mass ($\xi_{dis}=\xi_{dis,cr}$) is dissolved and corresponds to the dissolution of all diagenetic bonds. $\xi_{dis,cr}$ represents the ideal threshold between the bonded and the unbonded granular material state.

Ciantia et al, 2015 show that the unbonded granular material develops into a depositional bonded structure when dried (state II in Fig. 2a).

2 The constitutive relationship.

The conceptual bases for the extension of the classical theory of plasticity to incorporate the effects of bonding and quantitatively describe the mechanical effects of bond degradation are already in the innovative works of Nova and coworkers (Nova, 1992; Gens and Nova, 1993; Lagioia and Nova, 1995). These authors introduced an additional set of “bonding-related" internal variables and described the mechanical bond degradation by means of suitable hardening rules. Subsequently they employed the same conceptual framework to phenomenologically handle chemical degradation of weak rocks due to weathering. (Nova, 1997, 2000; Tamagnini et al., 2002; Nova et al., 2003).

The constitutive model presented in this work, capable of describing i) the instantaneous drop of strength and stiffness upon saturation, ii) the mechanical consequences of the subsequent long term debonding process, and iii) the dissolution induced chemical deformations (Ciantia et al, 2014), differently from what done so far, accounts for the mechanical consequences of hydro-chemical bond degradation by means of simplified multiscale approaches. To ease the reading of the paper, the constitutive model conceived by Nova et al, 2003, is summarized in section 2.1. In section 2.2 a modified hardening rule (to capture the mechanical consequences of STD and LTD) is introduced. In section 2.3 the hydro – chemical damage effects are incorporated by means of a damage variable related to the evolution of the bond geometry. Finally, in section 2.4 the chemical deformations, developing as a consequence of dissolution, once the material is turned into its granular state ($\xi_{dis} > \xi_{dis,cr}$), are integrated by adding an irreversible chemical contribution to the strain rate tensor.

2.1 The Nova Model

Isotropic strain hardening elasto-plastic constitutive models, conceived in order to reproduce the mechanical consequences of hydro-chemo-mechanical processes usually assume the total strain rate tensor ($\dot{\boldsymbol{\varepsilon}}$) to be additively decomposed into an *elastic*, reversible component ($\dot{\boldsymbol{\varepsilon}}^e$) and a *plastic* irreversible one ($\dot{\boldsymbol{\varepsilon}}^p$); the (hyper)elastic stiffness tensor ($\boldsymbol{D}^e$) to be derived from a suitably defined *stored energy function* $\psi(\boldsymbol{\varepsilon}^e)$; the stresses belonging to a *convex* set $\mathbb{E}_\sigma$, defined as $\mathbb{E}_\sigma := \left\{(\boldsymbol{\sigma},\boldsymbol{q}) \,\middle|\, f(\boldsymbol{\sigma},\boldsymbol{q}) \le 0\right\}$ where $\boldsymbol{\sigma}$ stands for the stress tensor, $f : \mathrm{Sym} \times \mathbb{R}^{n_{\mathrm{int}}} \mapsto \mathbb{R}$ is a convex function known as *yield function*, while $\boldsymbol{q} \in \mathbb{R}^{n_{\mathrm{int}}}$ is the vector of internal variables; the plastic strain rate tensor to be obtained by imposing the so called *flow rule* through the definition of a *plastic potential* $g : \mathrm{Sym} \times \mathbb{R}^{n_{\mathrm{int}}} \mapsto \mathbb{R}$ and a *plastic multiplier* $\dot{\Lambda}$; the evolution of the internal variables $\boldsymbol{q}$, to be governed by both mechanical and chemical processes (Nova et al 2003). In particular the mechanical consequences of the chemical processes are taken into account by means of an externally controlled degradation function $Y : \mathbb{R} \mapsto \mathbb{R}$ phenomenologically calibrated.

The analytical expression for both the yield function and plastic potential of the Nova Model are the ones proposed by Lagioia et al. (1995). The intersection of $f = 0$ with the positive and negative p axis are called $p_c = p_s + p_m$ and p_t, respectively. p_s plays the role of a sort of preconsolidation pressure, as it is for soils. In the Nova Model p_s is assumed to depend on both the plastic volumetric $\dot{\varepsilon}_v^p$ and deviatoric $\dot{\varepsilon}_s^p$ strain rates as it follows:

$$\dot{p}_s = \rho_s p_s \left(\dot{\varepsilon}_v^p + \zeta_s \dot{\varepsilon}_s^p\right) \tag{3}$$

where ρ_s and ζ_s are constitutive parameters. In contrast, p_t and p_m account for the effects of interparticle bonding. The existence of bonds therefore implies: (i) a non-zero tensile strength (p_t>0) (di Prisco et al, 1992, Gens & Nova, 1993, Arroyo et al 2012) and (ii) an increase in the yield stress along radial loading paths. p_m corresponds to such an increase in case of an isotropic compression path. Although the quantities p_m and p_t can be in general considered as two independent hardening variables, they are usually assumed to be related to each other by the simple proportional rule (p_t=k p_m). Finally to incorporate weathering Nova and co-workers (Nova et al, 2003) redefined p_m and p_t as it follows:

$$p_t := p_t\left(\varepsilon_{ij}^p, X_d\right) = P_t\left(\varepsilon_{ij}^p\right) Y\left(X_d\right) = P_t Y \tag{4}$$

where $P_t\left(\varepsilon_{ij}^p\right)$ is a scalar function decreasing monotonically with plastic strains whereas $Y\left(X_d\right)$ is a phenomenologically calibrated scalar function decreasing from 1 to 0 with X_d: a convenient scalar measure of the degree of weathering (Lumb, 1962). In the rate form, the vector of internal variables $\boldsymbol{q} := \left\{p_s, p_t\right\}$, reads:

$$\dot{\boldsymbol{q}} = \dot{\Lambda}\boldsymbol{h}\left(\boldsymbol{\sigma}, \boldsymbol{q}, Y\right) + \dot{Y}\boldsymbol{\eta}\left(\boldsymbol{\sigma}, \boldsymbol{q}, Y\right) \tag{5}$$

where

$$\boldsymbol{h} = \begin{Bmatrix} \rho_s p_s \left(tr\left(\dfrac{\partial g}{\partial \boldsymbol{\sigma}}\right) + \zeta_s \sqrt{\dfrac{2}{3}} \left\| \mathrm{dev}\left(\dfrac{\partial g}{\partial \boldsymbol{\sigma}}\right) \right\| \right) \\ -\rho_t p_t \left(\left| tr\left(\dfrac{\partial g}{\partial \boldsymbol{\sigma}}\right) \right| + \zeta_t \sqrt{\dfrac{2}{3}} \left\| \mathrm{dev}\left(\dfrac{\partial g}{\partial \boldsymbol{\sigma}}\right) \right\| \right) \end{Bmatrix} \qquad \boldsymbol{\eta} = \begin{Bmatrix} 0 \\ p_t / Y \end{Bmatrix} \tag{6}$$

and ρ_t, ρ_s, ζ_s and ζ_t are constitutive parameters

2.2 Redefinition of the weathering function *Y*.

In this section, the Nova empirically based weathering function $Y(X_d)$, is redefined by accounting for the above introduced STD and LTD mechanisms. This is done by using a multiscale approach allowing the authors to write the weathering function, Y, as a function of both ξ_{sus} and ξ_{dis}. This objective is obtained by assuming the variations in the macroscopic strength and deformability experienced by the material to be the consequence, from a microstructural viewpoint, of a reduction in the bond sectional area. To schematically implement this approach, the simplified geometry of Fig. 3 can be thus taken into consideration. The tensile force transmitted by the bonds can be assumed to be proportional (i) to the mean cross-sectional area of both diagenetic and depositional bonds ($A_{b,dia}$ and $A_{b,dep}$) and (ii) to the tensile strength (evaluated at the micro-scale) ($\bar{\sigma}$) of the material assumed to be independent of the type of bond, but affected by irreversible strains. Therefore:

$$p_t = p_t\left(\bar{\sigma}, A_{b,dia}, A_{b,dep}, \mathrm{X}'\right) \tag{7}$$

where X' is an up-scaling function depending on the geometrical configuration of the microstructure. By assuming the representative elementary volume (REV) to be a periodic repetition of both diagenetic and depositional bonds (Fig. 3d), the following simplified upscaling relation can be written:

$$\begin{aligned} p_t &= \mathrm{X}'\bar{\sigma}\left(\frac{n_{dia}A_{b,dia}}{A_{rev}^{MACRO}} + \frac{n_{dep}A_{b,dep}}{A_{rev}^{MACRO}}\right) = \mathrm{X}\bar{\sigma}\left(\frac{n_{dia}A_{b,dia}}{n_{gr}A_{gr}} + \frac{n_{dep}A_{b,dep}}{n_{gr}A_{gr}}\right) = \\ &= \mathrm{X}\bar{\sigma}\left[\bar{Y}_{dis}\left(\xi_{dis}\right) + \bar{Y}_{sus}\left(\xi_{sus}\right)\right] \end{aligned} \tag{8}$$

where n_{dia} and n_{dep} stand for the number of diagenetic and depositional bonds in the macro-REV along the direction of the macro-tensile stress, respectively; whereas A_{rev}^{MACRO} is the cross-section area of the macro-REV along which the stress is acting. The upscaling

function X' is modified to X in order to account for the material porosity and, owing to the hypothesis of periodic repetition of the REV, to write A_{rev}^{MACRO} (Fig. 3) as the cross-sectional area of a grain A_{gr} (of radius R_0) taken n_{gr} times, where n_{gr} represents the number of grains forming the macro REV. As was previously mentioned ξ_{sus} and ξ_{dis} are strictly related to the depositional and diagenetic bond area evolution, respectively. Therefore in (8) $\overline{Y}_{dis}$ depends exclusively on the amount of dissolved mass (ξ_{dis}) since the diagenetic bond area is assumed to solely change for chemical dissolution effects (LTD), whereas $\overline{Y}_{sus}$ depends on both the amount of powder forming depositional bonds (ξ_{sus}) controlling the depositional bond area evolution (STD). By indicating with

$$\overline{Y} = \overline{Y}_{dis} + \overline{Y}_{sus} \tag{9}$$

and by substituting eq (4)a and (9) into eq.(8) we obtain:

$$P_t Y = \mathrm{X}\overline{\sigma}\overline{Y} \tag{10}$$

where $\overline{Y}$ and Y are the micro and macro scale weathering functions, respectively.

2.2.1 Hydro-chemo induced bond area evolution: the microscale weathering function

By assuming a circular cross sectional area for the bonds, the two ratios appearing in eq. (8) become:

$$\begin{cases} \overline{Y}_{dis} = \dfrac{n_{dia}}{n_{gr}} \dfrac{\pi\left(r_{0,dia} - d_{dia}\right)^2}{\pi R_0^2} \\ \overline{Y}_{sus} = \dfrac{n_{dep}}{n_{gr}} \dfrac{\pi\left(r_{0,dep} - d_{dep}\right)^2}{\pi R_0^2} \end{cases} \tag{11}$$

where the first and the second lines of eq. (11) represent the counterpart of strength provided by the diagenetic and depositional bonds, respectively. By interpreting, for the sake of simplicity, the dissolution as an isotropic thinning of the calcarenite, the variation in the volume of the solid can be expressed as it follows:

$$d(t) := \frac{\Delta V_s}{A} = \frac{\Delta M}{\rho A} \tag{12}$$

where $d(t)$ represents the thickness of the dissolved layer of volume ΔV_s at a given instant of time (Fig. 3), A corresponds to the reacting surface area, ρ is the calcite density and by substituting eq (2) into (12) we obtain:

$$d(t) = \frac{\xi_{dis} M_0}{\rho A} = \frac{\xi_{dis} \rho_s V_{s0}}{\rho_s A} = \frac{\xi_{dis}}{A^*} \tag{13}$$

where A^* is the specific surface area in cm^2/cm^3 of the material. By indicating with $\xi_{dis,cr}$ the value of ξ_{dis} corresponding to the dissolution of all the bonds, ($\xi_{dis} = \xi_{dis,cr}$ occurs when $d=r_{0,dia}$) A^* can be expressed as $\xi_{dis,cr} / r_{0,dia}$ and by substituting eq. (13) into eq.(11):

$$\overline{Y}_{dis} = \begin{cases} \dfrac{r_{0,dia}^2 n_{dia}}{R_0^2 n_{gr}} \left(1 - 2\dfrac{\xi_{dis}}{\xi_{dis,cr}} + \dfrac{\xi_{dis}^2}{\xi_{dis,cr}^2} \right) & \xi_{dis} \le \xi_{dis,cr} \\ 0 & \xi_{dis} > \xi_{dis,cr} \end{cases} \tag{14}$$

Analogously in case of STD:

$$\overline{Y}_{sus} = \frac{r_{0,dep}^2 n_{dep}}{R_0^2 n_{gr}} \left(1 - 2\xi_{sus} + \xi_{sus}^2 \right) \tag{15}$$

where the critical value of suspended mass is equal to unity ($\xi_{sus,cr}$=1) since all the powder needs to suspend for STD to be complete. Eq. (9) thus becomes:

$$\overline{Y} = \overline{Y}_{dis} + \overline{Y}_{sus} = \begin{cases} \frac{r_{0,dia}^2 n_{dia}}{R_0^2 n_{gr}} \left(1 + \frac{\xi_{dis}^2}{\xi_{dis,cr}^2} - \frac{2\xi_{dis}}{\xi_{dis,cr}} \right) + \frac{r_{0,sus}^2 n_{dep}}{R_0^2 n_{gr}} \left(1 + \xi_{sus}^2 - 2\xi_{sus} \right) & \xi_{dis} \le \xi_{dis,cr} \\ \frac{r_{0,sus}^2 n_{dep}}{R_0^2 n_{gr}} \left(1 + \xi_{sus}^2 - 2\xi_{sus} \right) & \xi_{dis} > \xi_{dis,cr} \end{cases} \quad (16)$$

Initially, when the material is intact and it hasn't experienced any dissolution induced damage ($\xi_{dis} = 0$), under both dry ($\xi_{sus} = 0$) and wet ($\xi_{sus} = 1$) conditions, the micro-scale weathering function (eq. (16)) simplifies to:

$$\begin{cases} \overline{Y}^w = \frac{r_{0,dia}^2 n_{dia}}{R_0^2 n} & \left(\xi_{dis} = 0 ; \xi_{sus} = 1 \right) \\ \overline{Y}^d = \frac{r_{0,dia}^2 n_{dia}}{R_0^2 n} + \frac{r_{0,sus}^2 n_{dep}}{R_0^2 n} & \left(\xi_{dis} = 0 ; \xi_{sus} = 0 \right) \end{cases} \quad (17)$$

where $\overline{Y}^d$ and $\overline{Y}^w$ stand for the micro-weathering functions under dry and wet conditions, respectively. The macroscale expression for the weathering function is thus obtained by correlating the two multiplying terms ($\frac{r_{0,dia}^2 n_{dia}}{R_0^2 n}$ and $\frac{r_{0,sus}^2 n_{dep}}{R_0^2 n}$) in eq. (16) describing the initial ideal geometry of the microstructure to macroscale properties of the material. To do so, as is detailed in section 2.2.2 a downscaling procedure is employed. Finally, in section 2.2.3, the evolution of ξ_{dis} and ξ_{sus} are described in terms of degree of saturation, S_r, and bulk fluid concentrations, [.], respectively.

2.2.2 Downscaling procedure: the macroscale weathering function

By substituting eq. (17) into eq.(10), the following relation can be obtained:

$$\begin{cases} \frac{r_{0,dia}^2 n_{dia}}{R_0^2 n} = \frac{P_t}{X\overline{\sigma}} Y^w \\ \frac{r_{0,dia}^2 n_{dia}}{R_0^2 n} + \frac{r_{0,sus}^2 n_{dep}}{R_0^2 n} = \frac{P_t}{X\overline{\sigma}} Y^d \end{cases} \quad (18)$$

where Y^d and Y^w represent the macro-weathering functions under dry and wet conditions, respectively. By using eq. (4) and considering a weathering induced (non-mechanical) evolution of the yield locus, by assuming an omothetical shrinkage for the yield function, it is thus possible to correlate p_t to the uniaxial compressive strength of the material at different levels of weathering (Fig. 4b). In particular under a dry intact state and under saturated conditions:

$$\begin{cases} Y^w = \dfrac{p_{t0}^w}{p_{t0}^d} = \dfrac{\sigma_{c0}^w}{\sigma_{c0}^d} \\ Y^d = \dfrac{p_{t0}^d}{p_{t0}^d} = 1 \end{cases} \tag{19}$$

where σ_{c0}^d, σ_{c0}^w, p_{t0}^d and p_{t0}^w are the initial uniaxial compression strength and the initial isotropic tensile strength of the material under dry and wet conditions, respectively. By substituting eq. (19) in (18) we finally derive:

$$\begin{cases} \dfrac{r_{0,dia}^2 n_{dia}}{R_0^2 n} = \dfrac{P_t}{\mathrm{X}\bar{\sigma}}\left(\dfrac{\sigma_{c0}^w}{\sigma_{c0}^d}\right) \\ \dfrac{r_{0,sus}^2 n_{dep}}{R_0^2 n} = \dfrac{P_t}{\mathrm{X}\bar{\sigma}}\left(1-\dfrac{\sigma_{c0}^w}{\sigma_{c0}^d}\right) \end{cases} \tag{20}$$

and by substituting eq. (20) into eq. (16) and by using eq.(10), the macro weathering function reads:

$$Y = Y_{dis} + Y_{sus} \tag{21}$$

where

$$Y_{dis} = \begin{cases} \dfrac{\sigma_{c0}^w}{\sigma_{c0}^d}\left(1 - \dfrac{2\xi_{dis}}{\xi_{dis,cr}} + \dfrac{\xi_{dis}^2}{\xi_{dis,cr}^2}\right) & \xi_{dis} \le \xi_{dis,cr} \\ 0 & \xi_{dis} > \xi_{dis,cr} \end{cases} \tag{22}$$

$$Y_{sus}=\left\{\frac{\sigma_{c0}^{d}\text{-}\sigma_{c0}^{w}}{\sigma_{c0}^{d}}\left(1\text{-}2\xi_{sus}+\xi_{sus}^{2}\right)\right. \tag{23}$$

2.2.3 Evolution of ξ_{dis} and ξ_{sus}

Ciantia & Hueckel 2013 proposed a simplified approach to account for the theoretical chemo-mechanical coupling mechanism induced by the micro-crack formation in saturated and stressed calcarenites. This enables to express $\dot{\xi}_{dis}$ as a function of ionic concentrations in the bulk fluid, [.], and volumetric plastic strain, ε_v^{pl}:

$$\frac{d\xi_{dis}}{dt}=f\left(K_{a,b},[.],\varepsilon_v^{pl}\right)=\begin{cases}K_b\left(\mathrm{C}-\left[\mathrm{Ca}^{2+}\right]^{\frac{1}{2}}\left[\mathrm{CO}_3^{2-}\right]^{\frac{1}{2}}\right)\left(1+\phi\varepsilon_v^{pl}\right) & pH>6.5\\ K_a\left[\mathrm{H}^{+}\right]\left(1+\phi\varepsilon_v^{pl}\right) & pH\le 6.5\end{cases} \tag{24}$$

where the square brackets [.] indicate the ionic concentration, C is an equilibrium constant (2.47e-7 mol/cm^3), ϕ is a chemo-mechanical coupling material parameter, while K_b and K_a are dissolution parameters. For a Gravina calcarenite these were also calibrated (K_b = 4e-3 and K_a = 63.8 cm^3/s mol respectively) (Ciantia & Hueckel 2013).

While ξ_{dis} is a directly measurable quantity, strictly depending on the kinetics of dissolution (Ciantia & Hueckel, 2013), as is detailed in Ciantia et al 2014, the experimental measure of ξ_{sus} and its evolution during STD is not possible. Thus, for the sake of simplicity, the authors decided to assume a bi-linear relation between ξ_{sus} and S_r:

$$\begin{cases}\xi_{sus}=1-\dfrac{M_P}{M_{P_0}}\left(1-\dfrac{S_r}{S_r^*}\right) & 0\le S_r\le S_r^*\\ \xi_{sus}=1 & S_r>S_r^*\end{cases} \tag{25}$$

where S_r* is the minimum degree of saturation necessary to suspend all the depositional bonds, M_{P_0} is the initial powder mass inside the structure and M_P is the current amount of powder mass. Therefore, by substituting (25) into (23) we get

$$Y_{sus} = \begin{cases} \dfrac{\sigma_{c0}^{d} - \sigma_{c0}^{w}}{\sigma_{c0}^{d}} \left(\dfrac{M_p}{M_{p0}}\right)^2 \left(1 - \dfrac{S_r}{S_r^*}\right)^2 & S_r \le S_r^* \\ 0 & S_r > S_r^* \end{cases} \tag{26}$$

In the above equation $\left(\frac{M_p}{M_{p0}}\right)$ is a function depending on the amount of powder mass present in the porous rock at a given instant of time. For a closed system the total powder mass remains constant, ($M_p = M_{p_0}$), while, if the system is open, the problem is dominated by the associated transport processes. Andriani and Walsh (2007) showed that with wetting and drying cycles in open systems (systems where the suspended mass can be expelled from the sample) the increase in strength upon redrying is not fully recovered. In what follows only closed systems are instead considered. Finally by differentiating eq. (21) we obtain

$$\dot{Y} = \Xi \dot{\xi}_{dis} + \Sigma \dot{S}_r \tag{27}$$

where

$$\Xi = \begin{cases} -2\dfrac{\sigma_{c0}^{w}}{\sigma_{c0}^{d}} \left(\dfrac{1}{\xi_{dis,cr}} - \dfrac{\xi_{dis}}{\xi_{dis,cr}^2}\right) & \xi_{dis} \le \xi_{dis,cr} \\ 0 & \xi_{dis} > \xi_{dis,cr} \end{cases}$$

$$\Sigma = \begin{cases} -\left(\dfrac{\sigma_{c0}^{d} - \sigma_{c0}^{w}}{\sigma_{c0}^{d}}\right) \left(\dfrac{1}{S_r^*} - \dfrac{S_r}{S_r^{*2}}\right) & S_r \le S_r^* \\ 0 & S_r > S_r^* \end{cases} \tag{28}$$

2.3 Hydro-Chemical damage: the stiffness weathering function Y_E

Differently from classical damage mechanics (Krajcinovic, 1989), where damage is assumed to be associated with the development of micro-discontinuities inducing an irreversible decay of mechanical properties, in this work a particular type of damage variable, only function on non-mechanical (hydro-chemo) processes, is introduced. In this model the damage variable is "reversible" since both drying (short-term) of the rock and diagenesis (long-term) induce the recovery of mechanical properties. The hydro-chemical effects on the elastic response of calcarenites are experimentaly described in Ciantia et al, (2014). In this model, these variations are assumed to affect only the material in its bonded state, while no stiffness variation due to chemical dissolution is considered for the carbonate rock in its unbonded conditions (p_t=0). The original (hyper)elastic relationship (Tamagnini et al, 2002) is here recast as,

$$\psi(\boldsymbol{\varepsilon}^e, D) = \psi_0(\boldsymbol{\varepsilon}^e)\left(1+\delta_b\left(1-D\right)\right) \tag{29}$$

where $\psi_0(\boldsymbol{\varepsilon}^e)$ is the elastic energy that the material would store under the case it was transformed into a granular assembly, δ_b is a constitutive parameter related to the extra stiffness caused by the presence of bonds and D is a damage scalar variable only dependent on non-mechanical effects. When bonds are completely dissolved and hence D=1, the original elastic response corresponding to the granular state is recovered. The damage variable D is formulated by using the isotropic damage introduced by Kachanov (1958) and applying the same multiscale approach adopted for the bond strength. In fact, analogously to what already illustrated for the description of the hardening variable p_t (eq. (8)), also the elastic behaviour of the material can be related to the bond cross-sectional area. This is done by introducing a

damage variable at the microscale, $\bar{D}$, and adopting the same upscaling-downscaling procedure used to define the evolution of p_t. The evolution of D is obtained in terms of Y_E, the stiffness weathering function, Y_E, depending exclusively on the amount of dissolved mass (ξ_{dis}) and the amount of powder forming depositional bonds (ξ_{sus}). Y_E is thus defined as:

$$\begin{cases} Y_E = (1-D) \\ Y_E = Y_{E,dis} + Y_{E,sus} \end{cases} \tag{30}$$

where

$$Y_{E,dis} = \begin{cases} \dfrac{E_0^w}{E_0^d}\left(1-\dfrac{\xi_{dis}}{\xi_{dis,cr}}\right)^2 & \xi_{dis} \le \xi_{dis,cr} \\ 0 & \xi_{dis} > \xi_{dis,cr} \end{cases} \tag{31}$$

and

$$Y_{E,sus} = \begin{cases} \dfrac{E_0^d - E_0^w}{E_0^d}\left(1-\dfrac{S_r}{S_r^*}\right)^2 & S_r \le S_r^* \\ 0 & S_r > S_r^* \end{cases} \tag{32}$$

where E_0^d and E_0^w represent the Young modulus for the intact material under dry end wet conditions, respectively. The mathematical developments of the multiscale procedure used to obtain eq. (31) and (32) are reported in Appendix A. In conclusion, the introduction of a damage variable for the definition of the stored energy function implies that:

$$\dot{\boldsymbol{\sigma}} = \boldsymbol{D}^e \dot{\boldsymbol{\varepsilon}}^e + \boldsymbol{D}_M \dot{Y}_E \tag{33}$$

where

$$\boldsymbol{D}^e = \frac{\partial^2 \psi_0(\boldsymbol{\varepsilon}^e)}{\partial \boldsymbol{\varepsilon}^e \otimes \partial \boldsymbol{\varepsilon}^e}\left(1+\delta_b Y_E\right) \tag{34}$$

$$\boldsymbol{D}_M = \frac{\partial \psi_0(\boldsymbol{\varepsilon}^e)}{\partial \boldsymbol{\varepsilon}^e} \cdot \delta_b \tag{35}$$

$$\dot{Y}_E = \Xi_E \dot{\xi}_{dis} + \Sigma_E \dot{S}_r \tag{36}$$

where

$$\begin{aligned} \Xi_E &= \begin{cases} -2\dfrac{E_0^w}{E_0^d}\left(\dfrac{1}{\xi_{dis,cr}} - \dfrac{\xi_{dis}}{\xi_{dis,cr}^2}\right) & \xi_{dis} \le \xi_{dis,cr} \\ 0 & \xi_{dis} > \xi_{dis,cr} \end{cases} \\ \Sigma_E &= \begin{cases} -\dfrac{E_0^d - E_0^w}{E_0^d}\left(\dfrac{1}{S_r^*} - \dfrac{S_r}{S_r^{*2}}\right) & S_r \le S_r^* \\ 0 & S_r > S_r^* \end{cases} \end{aligned} \tag{37}$$

and $\psi_0(\boldsymbol{\varepsilon}^e)$ is taken from Tamagnini et al, (2002). In this work the hyperelastic parameters p_r and $\hat{k}$ will be chosen to obtain an equivalent linear elastic relationship and, as is detailed in (Tamagnini et al, 2002), this goal is achieved by fixing a very high value to p_r and calculating the $\hat{k}$ best fitting the experimental data. By looking at eq. (33), it is worth noting that as the bond cross sectional area decreases in size owing to suspension of depositional bonds and/or dissolution of diagenetic bonds, the hydro chemical damage process evolves ($\dot{Y}_E \neq 0$) and chemical induced elastic deformations are developed ($\dot{\boldsymbol{\varepsilon}}^e \neq 0$) even for constant stress conditions.

2.4 Chemical deformations

When grains are dissolved, at a macroscopic level, irreversible strains develop and this is mainly true once the material is turned into its granular state ($\xi_{dis} > \xi_{dis,cr}$). To take this process into account in the framework of strain hardening elasto-plasticity an irreversible chemical strain rate contribution $\dot{\boldsymbol{\varepsilon}}^c$ is added:

$$\dot{\boldsymbol{\varepsilon}} = \dot{\boldsymbol{\varepsilon}}^{e} + \dot{\boldsymbol{\varepsilon}}^{p} + \dot{\boldsymbol{\varepsilon}}^{c} \tag{38}$$

In this section simple micro-scale conceptual considerations are employed to relate $\dot{\boldsymbol{\varepsilon}}^{c}$ to the amount of the dissolved mass. For the sake of clarity, we have to distinguish the case of granular assemblies from the case of bonded materials. In the first case, dissolution can induce a rearrangement of grains resulting essentially in the accumulation of irreversible deformations, $\dot{\boldsymbol{\varepsilon}}^{c} \neq 0$ (Fig. 5). In contrast, the same process does not occur in case of bonded materials. In a bonded material, the grain rearrangement is in fact prevented by the bonds themselves, $\dot{\boldsymbol{\varepsilon}}^{c} = 0$ (Fig. 6). In this work, chemical deformations are assumed to be solely volumetric, ε_{v}^{c}, and are calculated as the ratio between the change in REV volume, ΔV_{REV}, and the initial REV volume, $V_{0,REV}$. By employing the microstructural ideal scheme of four tangent spheres (2D view in Fig. 5), by means of eq. (13) and neglecting second order effects:

$$\varepsilon_{v}^{c} = \frac{\Delta V_{REV}}{V_{0,REV}} = \frac{6L_0^2 d - 12L_0 d^2 + 8d^3}{L_0^3} \approx \frac{6d}{L_0} = \frac{6\xi_{diss}}{A^* L_0} = \frac{6\xi_{diss}}{\frac{A}{V_{s0}} L_0} = \frac{6\xi_{diss}}{\frac{4\pi\left(L_0/2\right)^2}{\frac{4}{3}\pi\left(L_0/2\right)^3} L_0} = \xi_{diss} \tag{39}$$

where L_0 is the size of the meso-REV (see Fig. 5). Here too, assuming the macroscale-REV as a periodic repetition of the meso-REV the chemical strain tensor can be thus defined as:

$$\boldsymbol{\varepsilon}^{c} = \frac{1}{3}\varepsilon_{v}^{c}\boldsymbol{1} \tag{40}$$

where $\boldsymbol{1}$ is the identity tensor and

$$\varepsilon_v^c = \begin{cases} 0 & \xi_{diss} < \xi_{diss,cr} \\ \xi_{diss} - \xi_{diss,cr} & \xi_{diss} \geq \xi_{diss,cr} \end{cases} \tag{41}$$

and thus:

$$\dot{\varepsilon}_v^c = \begin{cases} 0 & \xi_{dis} < \xi_{dis,cr} \\ \dot{\xi}_{dis} & \xi_{dis} \geq \xi_{dis,cr} \end{cases} \tag{42}$$

As dissolution proceeds (line A-B in Fig. 7) no chemical strains are initially experienced by the material due to the presence of diagenetic bonds. However, once all the bonds are dissolved ($\xi_{diss} = \xi_{diss,cr}$) further dissolution causes irreversible chemical strains. It is clear that the rate of chemical volumetric strains, eq.(42), has a direct relationship with the dissolution rate equation, and hence the time derivative is done with respect to the physical time (Ciantia and Hueckel, 2013). As was suggested by equations (40) and (42), the rate of chemical strains is a discontinuous function of $\dot{\xi}_{diss}$. In order to avoid such a discontinuity, in the numerical code eq (41) has been defined as:

$$\dot{\varepsilon}^c = \boldsymbol{I} C \dot{\xi}_{dis} \tag{43}$$

where

$$C = \begin{cases} 0 & \xi_{dis} < \xi_{dis,cr} - \delta_\xi \\ \frac{1}{6}\left[\left\{1+\sin\left(\frac{\pi\xi_{dis}}{2\delta_\xi}\right)\right\}+\cos\left(\frac{\pi\xi_{dis}}{2\delta_\xi}\right)\left(\xi_{dis}-\xi_{dis,cr}\right)\right] & \xi_{dis,cr}-\delta_\xi \leq \xi_{dis} \leq \xi_{dis,cr}+\delta_\xi \\ \frac{1}{3} & \xi_{dis} > \xi_{dis,cr} - \delta_\xi \end{cases} \tag{44}$$

is a smoothing function ranging gradually from 0 to 1/3 and δ_ξ is a material parameter defining the magnitude of the transition zone.

2.5 General formulation

It is known that capillarity effects have a negligible effect on the mechanical behaviour of calcarenites, chalks and other carbonate porous rocks (Papamichos et al, 1997, Risnes and Flaageng 1999 and Risnes et al. 2005, Ciantia et al, 2014) as the apparent cohesion induced by capillary bridges can be neglected with respect to the natural cementation of the material. Therefore, following Hickman et al, 2008, the model here illustrated is developed in terms of conventional effective stresses neglecting the role of matric suction when the material behaves in partially saturated conditions. In other words in the following, according to the previous assumption:

$$\sigma'_{ij} = \sigma_{ij} - u^* \delta_{ij} \tag{45}$$

where

$$u^* = \begin{cases} 0 & 0 \le S_r < 1 \\ u_w & S_r = 1 \end{cases} \tag{46}$$

and u_w is the water pressure. By omitting the standard apex notation identifying the effective stress the constitutive relationship can be written as follows:

$$\dot{\sigma}_{ij} = D^{ep}_{ijhk}\dot{\varepsilon}_{hk} + \left(D^{LTD}_{ij} + D^{DAMAGE-dia}_{ij} + D^{GDP}_{ij}\right)\dot{\xi}_{dis} + \left(D^{STD}_{ij} + D^{DAMAGE-dep}_{ij}\right)\dot{S}_r \tag{47}$$

Or, by substituting eq. (24) into (47) to highlight the time dependence of the constitutive relationship:

$$d\sigma_{ij} = D^{ep}_{ijhk} d\varepsilon_{hk} + \left(D^{LTD}_{ij} + D^{DAMAGE-dia}_{ij} + D^{GDP}_{ij} \right) f\left(K_{a,b}, [.], \varepsilon^{pl}_{v} \right) dt + \\ + \left(D^{STD}_{ij} + D^{DAMAGE-dep}_{ij} \right) dS_r \tag{48}$$

where the analytical expressions of D^{ep}_{ijhk}, D^{LTD}_{ij}, $D^{DAMAGE-dia}_{ij}$, D^{GDP}_{ij}, D^{STD}_{ij}, and $D^{DAMAGE-dep}_{ij}$ are in Appendix B. The constitutive relation (eq. (48)) was integrated by means of an explicit integration scheme by employing an adaptive Runge-Kutta-Felhberg method of the third order (RKF-23), see (Stoer & Bulirsch, 1992).

3 Calibration procedure

The Macro and Micro experimental data presented in Ciantia et al (2014a,b) were used to calibrate the 24 constitutive parameters introduced above:

a_f, m_f, M_{fc}, M_{fe} concerning the yield surface shape, p_{s0}, p_{t0}, p_{m0} the yield surface initial size, a_g, m_g, M_{gc}, M_{ge} the plastic potential, ρ_s, ζ_s, ρ_t, ζ_t the mechanical hardening rule, $\xi_{dis,cr}$, S_r^*, σ_{c0}^d, σ_{c0}^w, E_0^d, E_0^w the weathering function and K_{gr}, ν, δ_b the elastic potential. We note that once the initial size of the yield locus is determined for both dry and wet conditions, once the elastic potential is calibrated, four of the weathering parameters (σ_{c0}^d, σ_{c0}^w, E_0^d and E_0^w) are also known making the independent parameters to calibrate 20.

In Fig. 8 the experimental test results concerning the yielding of a Gravina Calcarenite are summarized and the calibrated yield functions are compared. The corresponding surface parameters are summarized in Table 1, where the initial value for p_s, p_t and p_m are also reported. p_{s0}=1000 kPa was determined by following the procedure presented by Lagioia and Nova (1995) and using the experimental isotropic compression test results on the Gravia Calcarenite used for this study.

The mechanical behavior of the Gravina di Puglia calcarenite has been intensively investigated by Lagioia during his PhD (Lagioia, 1994). For this reason, both plastic potential and mechanical destructuration material parametres proposed by Lagioia et al. (1996) and Lagioia and Nova (1995), respectively have been used. Only the value of ζ_t, that is here set to one (Table 2), in order to better fit our triaxial compression test (Fig. 9), was changed.

$\xi_{dis,cr}$, S_r^*, σ_{c0}^d, σ_{c0}^w, E_0^d, E_0^w were already experimentally calibrated in Ciantia et al (2014a,b). Their values are summarized in Table 3. The only remaining elastic parameters to calibrated are K_{gr}, δ_b and ν.

K_{gr} is evaluated from oedometric test results when the material is totally debonded (Fig. 10a). δ_b can be assessed by employing the following equation:

$$K/K_{gr} = \left(1+\delta_b Y_E\right) \tag{49}$$

Were K is the oedometric stiffness corresponding to a certain degradation stage, defined by Y_E. In particular under either dry or wet intact conditions, $K = K_0^d$ and K_0^w respectively (Fig. 10a). By reporting on the K/K_0^d - Y_E plane the experimental results the value of δ_b can be easily derived (Fig. 10b). The Poisson ratio ν is determined by relating the intact oedometric stiffness K_0^d to the intact Young modulus E_0^d ($E_0^d = \left(1+\nu\right)\left(1-2\nu\right)\left(1-\nu\right)^{-1} K_0^d$). By assuming ν to be constant, also the Young modulus E may be used to derive δ_b. The calibrated parameters are summarized in Table 4.

4 Model Validation

4.1 Uncoupled hydro-chemo-mechanical tests

To validate both the mechanical hardening and plastic potential parameters, the oedometric compression tests on dry and wet Gravina Calcarenite samples were employed (Fig. 11). The experimentally observed post yielding plateau is not captured in a satisfactory way by the model because in this phase of the test, compaction bands develop within the specimen (Arroyo et al, 2005, Castellanza et al., 2009b; Dattola et al, 2014, Buscarnera and Laverack, 2014), while the simulations assume the sample not to localize. Nevertheless the mechanical hardening and plastic potential parameters calibrated in the previous section by means of a triaxial compression test are sufficiently good to fit the mechanical behavior of the calcarenite when loaded in oedometric conditions.

In Fig. 12 the weathering function *Y*, derived by the authors by means of the multiscale approach previously described, is compared with the experimental results by Ciantia et al 2014. The good agreement between experimental data and the model results validates the upscaling procedure and in particular the hydro-chemo-micromechanical assumptions made in defining the bond meso-REV scheme and the bond area evolution (§ 2.2). In Fig. 12a the 3D graphical representation highlights the short and the long term weathering processes: the first evolving with saturation on the plane $\xi_{dis} = 0$ and the second evolving with ξ_{dis} on the plane S_r=1. Analogously, in Fig. 13, another series of numerical simulations, highlighting the dependence of both strength and stiffness on the dissolved mass in terms of ξ_{dis}, is compared with the experimental evidence. Here too, the good agreement supports the aforementioned multiscale procedure.

4.2 Coupled hydro-chemo-mechanical experiments

The *weathering tests* described in Ciantia et al 2014, carried out by means of the *WTD* and the creep test device under accelerated weathering conditions have been numerically simulated to validate the model. In particular four hydro-chemo-mechanical coupled test results have been simulated:

The first concerns the STD process only and consists in reproducing the failure of a dry pillar when saturated with water. The second concerns both STD and LTD processes. The test is identical to the previous one but, in this case, failure is not caused by the saturation induced weakening but by the long term dissolution of diagenetic bonds.

The third simulates a test where the LTD process does not cause the failure of the material (oedometric conditions) and the experiment continues also after the chemical induced yielding. Finally in the last experiment the GDP is investigated as dissolution induced volumetric deformations of a granular soluble material are studied. The reference material is a soil composed by clusters of calcarenite. This experiment validates the approach used to incorporate chemical deformations.

4.2.1 Saturation induced failure in weathering creep tests

A detailed description of this test is Ciantia et al, 2014: a dry cylinder of calcarenite is saturated by water under a constant uniaxial vertical load. In Fig. 14 numerical results are compared with experimental data. The dry material is first loaded up to a stress state that exceeds its ultimate wet strength and subsequently the sample is saturated. During saturation, which starts at point A, the material deforms as the vertical load is kept constant but the

elastic stiffness drops due to the STD process. At the same time the strength of the material decreases and in this case the strength drop induces the failure (point B).

4.2.2 Long term debonding induced failure in weathering creep tests

In this case both STD and LTD processes take place. After saturation, the material stress state still lies within the current wet yield locus. For this reason, failure will be reached only subsequently, when an acid flux of 3.7 mean pH attacks the material. In Fig. 15 the experimental results are compared with numerical simulations in terms of mean vertical strain (a), stress path (b) and stress strain curve (c). It is worth noting that the effects induced by both STD and LTD processes are captured by the model in a satisfactory way.

4.2.3 Oedometric weathering test on calcarenite

Also in this case, a detailed description of the test here numerically simulated is in Ciantia et al, 2014. As it was for the previous tests, in principle the test should be interpreted as a small scale boundary value problem. In fact, the in - and the out - fluid pH are different: the weathering function should assume different values across the specimen. Nevertheless, hereafter the numerical simulations assume the sample to be a REV. Three tests are here considered, these characterised by a pH of 3.65, 3.75 and 3.85. The chosen values fluctuate around the mean of the in - and the out - pH measured experimentally (Fig. 16a). Since $[H^+]$ is function of pH, by employing eq. (24) the accumulated dissolved mass can be estimated (Fig. 16b).

As is evident in Fig. 17a, the *loading phase* is simulated by imposing a constant rate to the axial stress until the final value of 2005 kPa is reached. The theoretical stress state in the

triaxial plane follows the linear path OA inside the initial elastic domain f_0^{dry}; both radial and axial stresses increase proportionally, as is expected in the case of an elastic material loaded under oedometric conditions.

Subsequently, the material is saturated *(saturation phase)* and both the axial stress and the radial strain are kept constant (σ_a=2005 kPa, $\varepsilon_r = 0$). In this case, the reduction in the elastic domain takes place in such a way that the stress level (point C) remains inside the yield locus of the intact wet rock, f_0^{wet}. As a consequence, no plastic strains develop. The material deforms because of the variation in the elastic stiffness induced by the STD process. After total saturation (point C) the *acid weathering phase* starts. Both the axial stress and the radial strain are still kept constant, S_r is maintained equal to one and an acid flux of constant pH (3.65, 3.75 and 3.85 for the three different tests) is imposed. The acid accelerates the dissolution process with a rate proportional to the imposed pH (eq. (24)) and hence ξ_{diss} increases with time. Here too, the hardening variables p_m and p_t and the stiffness of the material are forced to reduce by the weathering function. The change in stress induced by the reduction in the elastic domain size takes place as it follows: initially, the radial stress and the axial strain are fixed to point C (end of saturation phase); then, when point C is reached by the yield locus which is shrinking (f_{yield}^{wet}), the material yields and plastic strains develop to restore consistency. Consequently, the internal variable p_s increases while p_m and p_t decrease monotonically (Fig. 17b). As is evident from Fig. 17a, the stress image point moves along a line with a slope of –1.5, which in the triaxial plane represents a locus at constant value of axial stress.

The process stops after about three hours of acid flux. Points D, D′ and D″ in Fig. 17 are related to the final state of the material in the case of pH equal to 3.65, 3.75 and 3.85, respectively. The elastic domain represented by the surface $f^{wet}_{damaged}$ in Fig. 17 concerns the 3.85 pH test and in Fig. 17c the simulation of the deviatoric stress against the deviatoric strain is presented. In Fig. 18 both numerical and experimental radial stresses and axial strains occurring during the whole experiment are compared. The agreement seems to be quite satisfactory.

On the other hand, the rapid changes (discontinuities) characterizing the experimental results are not captured by the model. These "jumps" are probably a direct consequence of instability phenomena occurring in the material during the test. It is well known that, as the highly porous structure dissolves, the material weakens until the constant vertical load cannot be sustained. Sometimes, owing to the particular microstructure of the material, axial strains localize along horizontal layers. This phenomenon is known as compaction banding (Arroyo et al, 2005, Castellanza et al., 2009b; Dattola et al, 2014, Buscarenara & Leverak, 2014). As the formation of a compaction band is a dynamic process, the jumps in vertical strains and the associated discontinuities in the radial stress are justified.

In Fig. 17c and Fig. 18, a good agreement in terms of variation in stresses and strains is evident. In particular the values calculated by the model at the end of the *saturation phase* (point C) are very satisfactory while at the end of the *weathering phase* (points D, D′ and D″) the discrepancy is probably due to the non-uniformity of the pH value across the specimen during the experimental test which cannot be captured by the numerical simulation which assumes the specimen as a unique REV.

In Fig. 19, weathering is also testified by the clockwise rotation of the plastic strain rate unit vectors which stops when the material is totally weathered.

4.2.4 Acid accelerated weathering of granular calcarenite (oedometric conditions)

This test refers to a stress controlled non-conventional oedometric test on a material that starts from unbonded conditions ($\xi_{dis,cr} = 0$, $p_{t0}=0$, $p_{s0} = 20$ kPa). The experiment, detailed in Ciantia et al, (2014), is subdivided into three different phases. The loading phase (O-A in Fig. 20) is performed under water saturated conditions. This is to prevent the results to be affected by the STD. Subsequently the creep phase (A-B) starts. Even if the vertical stress is kept constant, both vertical strains and radial stresses increase. After about one hour, when the strain rates become negligible, a 2.4 l/h flux of 2.5 pH acid is imposed from the bottom. As was expected, grain dissolution process induces chemical deformations, decrease in the radial stresses, while vertical strains rapidly evolve (B-C). After one hour of acid flux the sample is washed with water (C-D). In this last phase both axial strains and radial stresses stop evolving (Fig. 20).

5 Conclusions

In this paper, a generalized strain hardening single potential elastoplastic constitutive model considering the hydro-chemo-mechanical coupling for soft porous rocks has been presented. The three elementary hydro-chemo- mechanical weathering processes i) short term debonding, STD; ii) long term debonding, LTD and iii) grain dissolution process GDP, experimentally observed occurring at the micro-scale are incorporated by means of a suitable

multiscale approach. Extended hardening laws, usually phenomenologically calibrated are micro-mechanically justified. Furthermore hydro-chemical damage has been introduced in the formulation by means of a scalar damage function. Even in this case its evolution is described by using a multiscale approach. To incorporate the dissolution induced chemical deformations experimentally observed once the soft rock is turned into a granular material, an additional strain rete tensor is introduced. The model has been validated by employing already published experimental data concerning different types of tests performed on Gravina calcarenite samples. The model has clearly shown to be capable of reproducing the mechanical consequences of the STD process. In case of both the LTD and GDP processes, physical time becomes an intrinsic variable of the model controlling the mechanical behavior of the material. Such feature gives to the proposed constitutive model the capability of predicting the temporal evolution of the mechanical response of soft carbonate rocks such as calcarenites.

6 Acknowledgments

The authors wish to thank Professor Tomasz Hueckel, Professor Claudio Tamagnini and Professor Riccardo Castellanza for the numerous fruitful discussions.

7 References:

Andriani, G. F. & Walsh, N. (2007). The effects of wetting and drying, and marine salt crystallization on calcarenite rocks used as building material in historic monuments. *Geological Society, London, Special Pubblications* **271**, 179-188.

Arroyo, M., Ciantia, M. O., Castellanza, R., Gens, A., Nova, R. (2012). Simulation of cement-improved clay structures with a bonded elasto-plastic model: A practical approach. *Computers and Geotechnics*, **45**, 140-150.

Arroyo, M., Castellanza, R., & Nova, R. (2005). Compaction bands and oedometric testing in cemented soils. Soils and foundations, 45(2), 181-194.

Buscarnera, G., & Laverack, R. T. (2014). Path dependence of the potential for compaction banding: Theoretical predictions based on a plasticity model for porous rocks. *Journal of Geophysical Research: Solid Earth*, *119*(3), 1882-1903

Castellanza, R., Parma, M., Pescatore, V. & Silvestro, G. (2009a). Model footing load tests on soft rocks. *Geotechnical Testing Journal* **32**, No. 3, 262 – 272

Castellanza, R., Gerolymatou, E. & Nova, R. (2009b) Experimental observations and modeling of compaction bands in oedometric tests on high porosity rocks. *Strain* **45**, 410–423

Ciantia, M. O., Castellanza, R., Crosta, G. B. & Hueckel, T. (2015), Effects of mineral suspension and dissolution on strenght and compressibility of soft carbonate rocks, Engineering Geology, **184,** 1–18

Ciantia, M. O., Castellanza, R., di Prisco, C. (2014), Experimental study on the water-induced weakening of calcarenites. ISSN 0723-2632 DOI 10.1007/s00603-014-0603-z (in press)

Ciantia, M. O., Hueckel, T. (2013). Weathering of stressed submerged calcarenites: chemo-mechanical coupling mechanisms, *Géothecnique*, **63** (9), 768–785

Ciantia, M. O. (2013). Multiscale hydro-chemo-mechanical modeling of the weathering of calcareous rocks:: An experimental, theoretical and numerical study. PhD thesis, Politecnico di Milano, Milan, Italy

Ciantia, M. O., Castellanza, R., di Prisco, C. & Hueckel, T. (2012). Experimental methodology for chemo-mechanical weathering of calcarenites. In Multiphysical testing of soils and shales (eds L. Laloui and A. Ferrari), pp. 331–336. Berlin/Heidelberg, Germany: Springer-Verlag.

Ciantia, M. O., Castellanza, R., di Prisco, C., (2013). Chemo-mechanical weathering of calcarenites: Experiments and theory. In Coupled Phenomena in Environmental Geotechnics (ads Manassero et al), pp. 541-548. Taylor & Francis Group, London,

Dattola, G., Prisco, C., Redaelli, I., & Utili, S. (2014). A distinct element method numerical investigation of compaction processes in highly porous cemented granular materials. *International Journal for Numerical and Analytical Methods in Geomechanics*.

De Groot, S., R. (1966). *Termodynamics of irriversible processes,* Amsterdam: North Holland.

Di Prisco, C., Matiotti, R., Nova, R. (1992), A mathematical model of grouted sand behaviour, *Proc*. *NUMOG IV*, Swansea, UK, Pande, G. and Pietrusczczak, S., Balkema, Rotterdam, 25-35.

Folk, R.L., 1959, Practical petrographic classification of limestones: American Association of Petroleum Geologists Bulletin, v. 43, p. 1-38

Gens, A., Nova, R. (1993). Conceptual bases for a constitutive model for bonded soils and weak rocks, *Hard Soils-Soft Rocks, Athens, Greece, Anagnostopoulos and others,* Balkema, Rotterdam, 485-494.

Gudehus G. Elastoplastische stoffgleichungen f .ur trockenen sand. Ingenieur-Archiv 1973; 42:151–169.

Hickman, R. J., Gutierrez, M. S., De Gennaro , V. and Delage, P. (2008) A model for pore-fluid-sensitive rock behavior using a weathering state parameter. *Int. J. Numer. Anal. Meth. Geomech.* 2008; **32**:1927–1953.

Krajcinovic, D. (1989). Damage mechanics. *Mechanics of materials*, *8*(2), 117-197.

Kachanov, L. M. (1958). Time of the rupture process under creep conditions. *Isv. Akad. Nauk. SSR. Otd Tekh. Nauk*, *8*, 26-31.

Lagioia, R. (1994), *Comportamento meccanico dei terreni cementati naturali: indagine sperimentale ed interpretazioni teoriche*, PhD Thesis, Politecnico di Milano, (in Italian).

Lagioia, R., Nova, R. (1995), An experimental and theoretical study of the behavior of a calcarenite in triaxial compression, *Géotechnique*, **45**, n. 4, 633-648.

Lagioia, R., Puzrin, A. M., & Potts, D. M. (1996). A new versatile expression for yield and plastic potential surfaces. *Computers and Geotechnics*, *19*(3), 171-191.

Lumb, P. (1962). The properties of decomposed granite. *Géotechnique.* **12**, 226-243.

Nova, R. (1997), On the modelling of the mechanical effects of diagenesis and weathering, *ISRM News Journal*, **4**, n. 2, 15-20.

Nova, R. (2000), Modelling the weathering effects on the mechanical behaviour of granite, *Constitutive Modelling of Granular Materials*, Horton, Greece, Kolymbas, D., Springer, Berlin, 397-411.

Nova, R., Castellanza, R. & Tamagnini, C. (2003). A constitutive model for bonded geomaterials subject to mechanical and or chemical degradation. *Int. J. Num. Anal. Meth. Geomech.* **27**, No. 9, 705-732.

Nova, R. (2012). *Soil mechanics*. John Wiley & Sons

Papamichos E, Brignoli M, Santarelli FJ. (1997) An experimental and theoretical study of a partially saturated collapsible rock. Mechanics of Cohesive-Frictional Materials; **2**:251–278.

Risnes R, Flaageng OF. Mechanical properties of chalk with emphasis on chalk–fluid interactions and micromechanical aspects. Oil and Gas Science and Technology 1999; 54(6):751–758.

Risnes R, Madland MV, Hole M, Kwabiah NK. Water weakening of chalk—mechanical effects of water–glycol mixtures. Journal of Petroleum Science and Engineering 2005; 48:21–36.

Simo JC, Hughes TJR. Computational Inelasticity. Springer: New York, 1997.

Stoer J, Bulirsch R. *Introduction to Numerical Analysis (2nd edn)*. Springer: New York, 1992

Tamagnini, C., Castellanza, R., & Nova, R. (2002). A generalized backward Euler algorithm for the numerical integration of an isotropic hardening elastoplastic model for mechanical and chemical degradation of bonded geomaterials. *International Journal for Numerical and Analytical Methods in Geomechanics*, *26*(10), 963-1004.

van Eekelen HAM. (1980) Isotropic yield surfaces in three dimensions for use in soil mechanics. International Journal for Numerical and Analytical Methods in Geomechanics; 4:89–101.

8 Tables

Table 1: Yield surface parameters and initial conditions

a_f	m_f	M_{fc}	M_{fe}	k	p_{s0}	p_{t0}
(–)	(–)	(–)	(–)	(–)	(kPa)	(kPa)
0.75	1.5	1.3	1.0	8±3	1000±200	350±100

Table 2: Plastic potential and mechanical hardening/softening parameters

Parameters	a_g	m_g	M_{gc}	M_{ge}	ρ_s	ζ_s	ρ_t	ζ_t
	(–)	(–)	(–)	(–)	(–)	(–)	(–)	(–)
Lagioia et. al, (1995, 1996)	1e-6	1.2	1.657	1.292	16.66	-0.1	15	1

Table 3: weathering parameters

$\xi_{dis,cr}$	S_r^*	σ_{c0}^d	σ_{c0}^w	E_0^d	E_0^w
(–)	(–)	(kPa)	(kPa)	(MPa)	(MPa)
0.4	0.3	2440±100	1760±100	315.0±100	150.0±50

Table 4: Elastic parameters

K_{gr}	ν	p_r	δ_b
(MPa)	(−)	(kPa)	(–)
40±5	0.09±0.02	1e+6	5±1

9 Figures

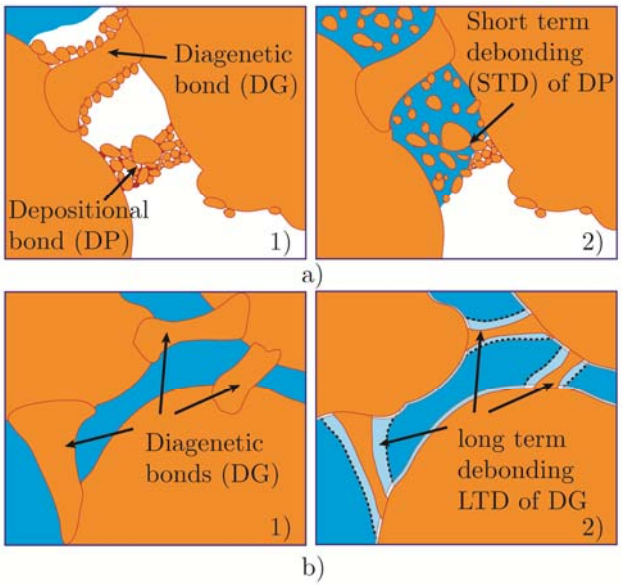

Fig. 1 Sketch of the material micro-structure: a) STD of DP bonds and b) LTD of DG bonds

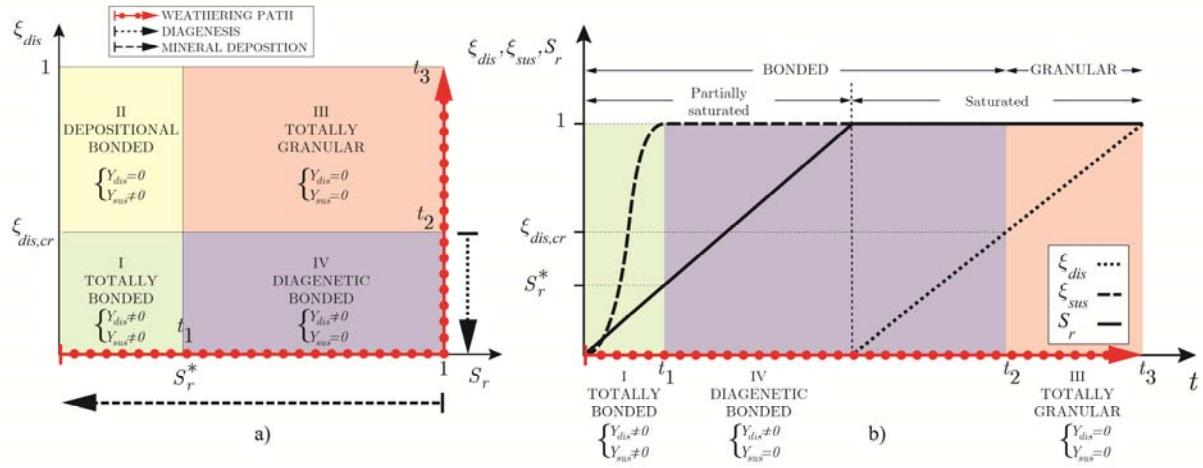

Fig. 2 Schematic representation of the STD, LTD and GDP processes: a) phase diagram of calcarenite in terms of S_r and ξ_{diss} b) Evolution of weathering in calcarenite (weathering path in a)) as a function of the state variables of the STD, LTD and GDP weathering processes.

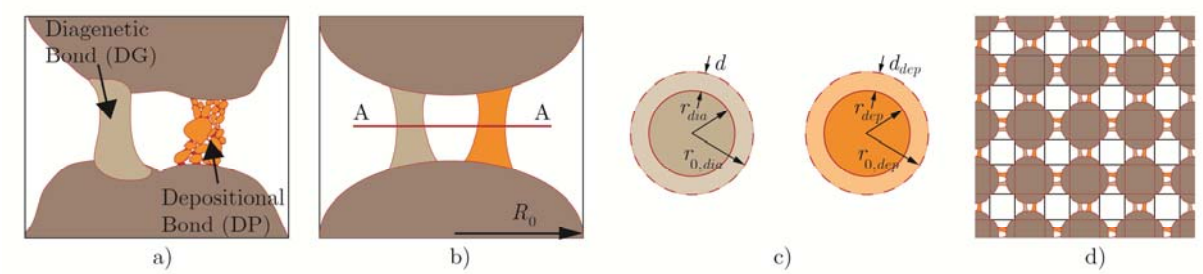

Fig. 3 Idealised microscopic schematic view of the material: a) diagenetic and depositional bonds, b) idealised geometry, c) cross-section A-A of the bonds and micro-variables definition, d) idealised porous microstructure.

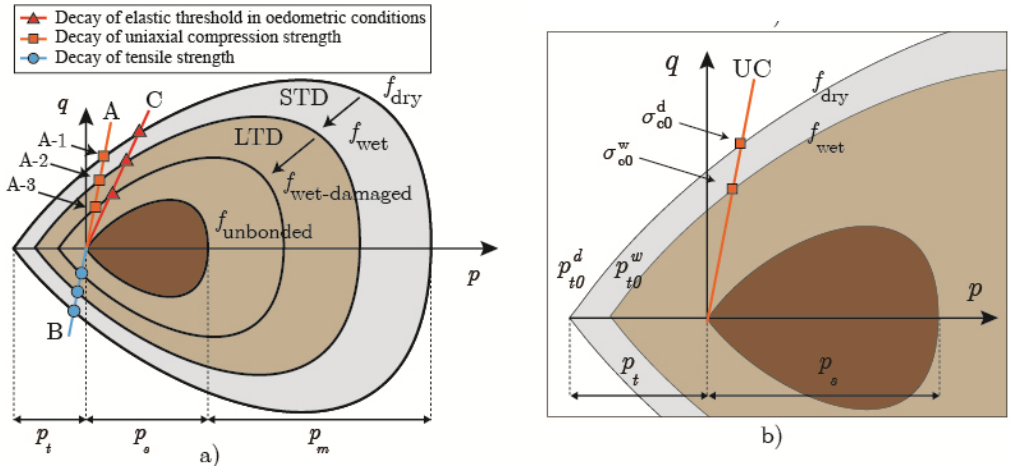

Fig. 4 a) Homothetic shrinkage of yield locus induced by STD and LTD and (b) zoom of tensile zone.

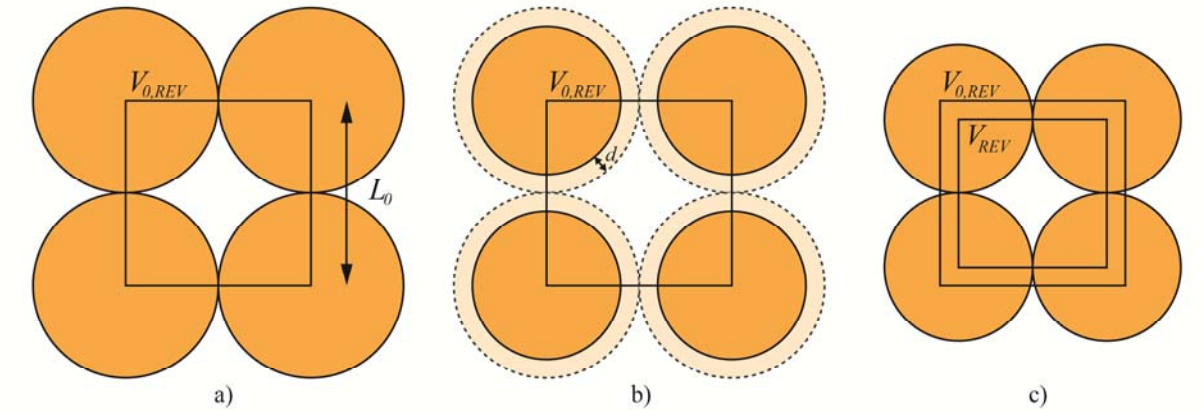

Fig. 5 Schematic representation of dissolution effects on unbonded soils

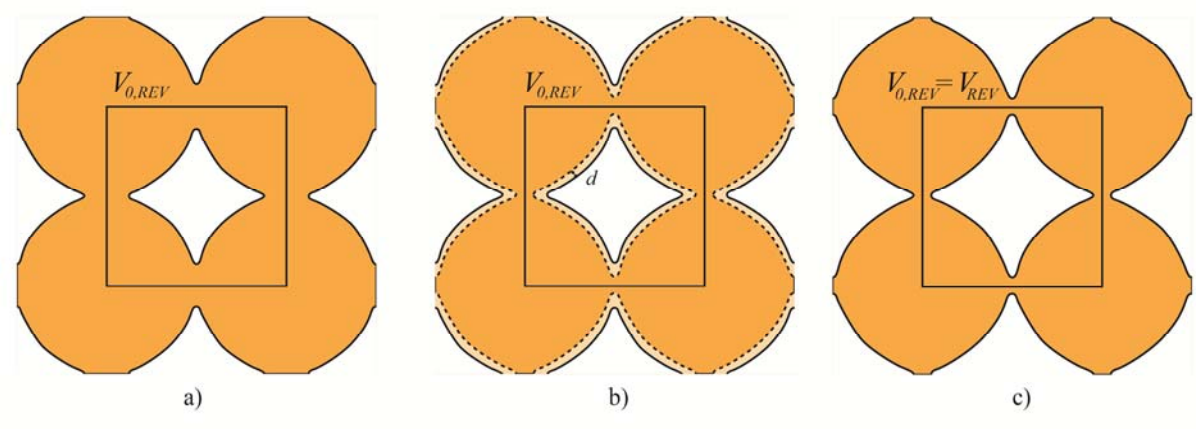

Fig. 6 Schematic representation of dissolution effects on bonded soft rocks

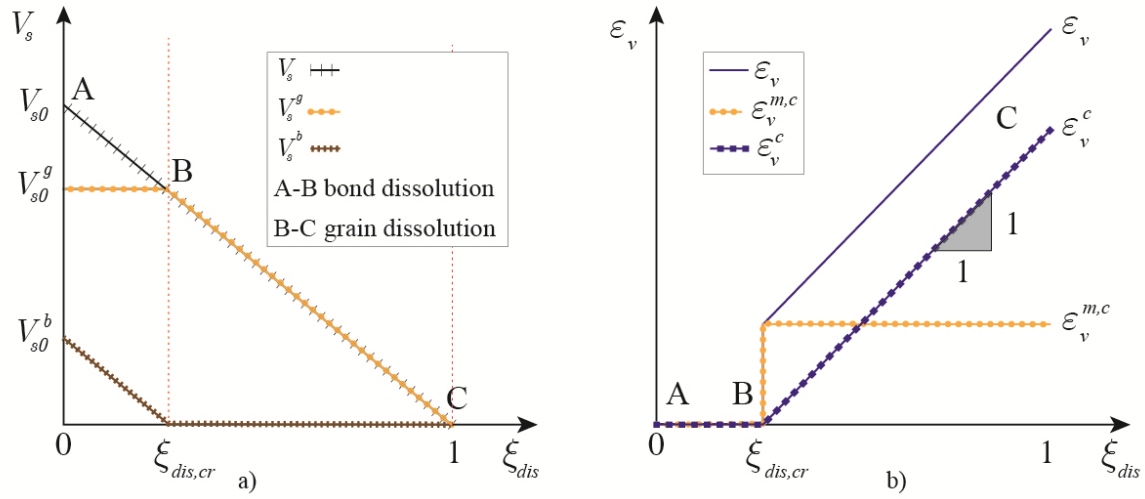

Fig. 7 : Definition of $\xi_{diss,cr}$: a) Solid volume variation and b) deformation with accumulated dissolved mass

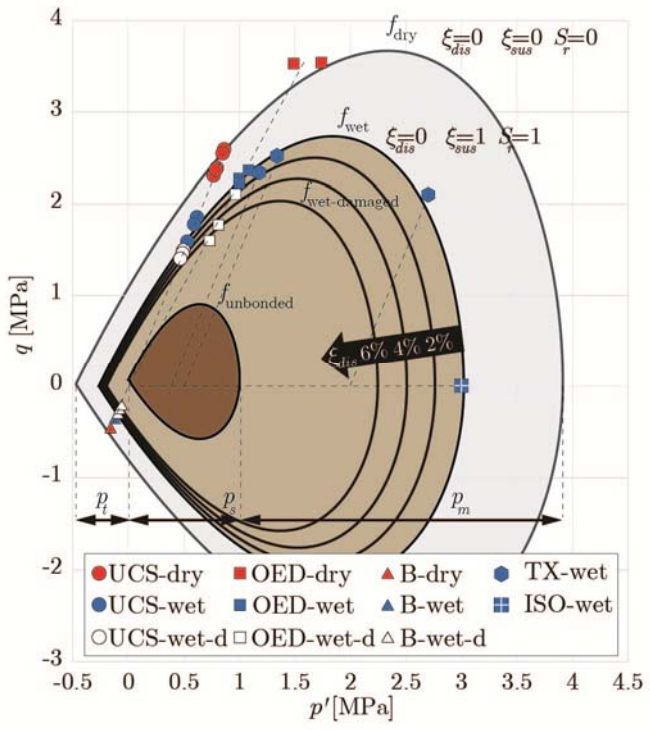

Fig. 8 Yield locus calibration: hydro-chemo weathering shrinkage

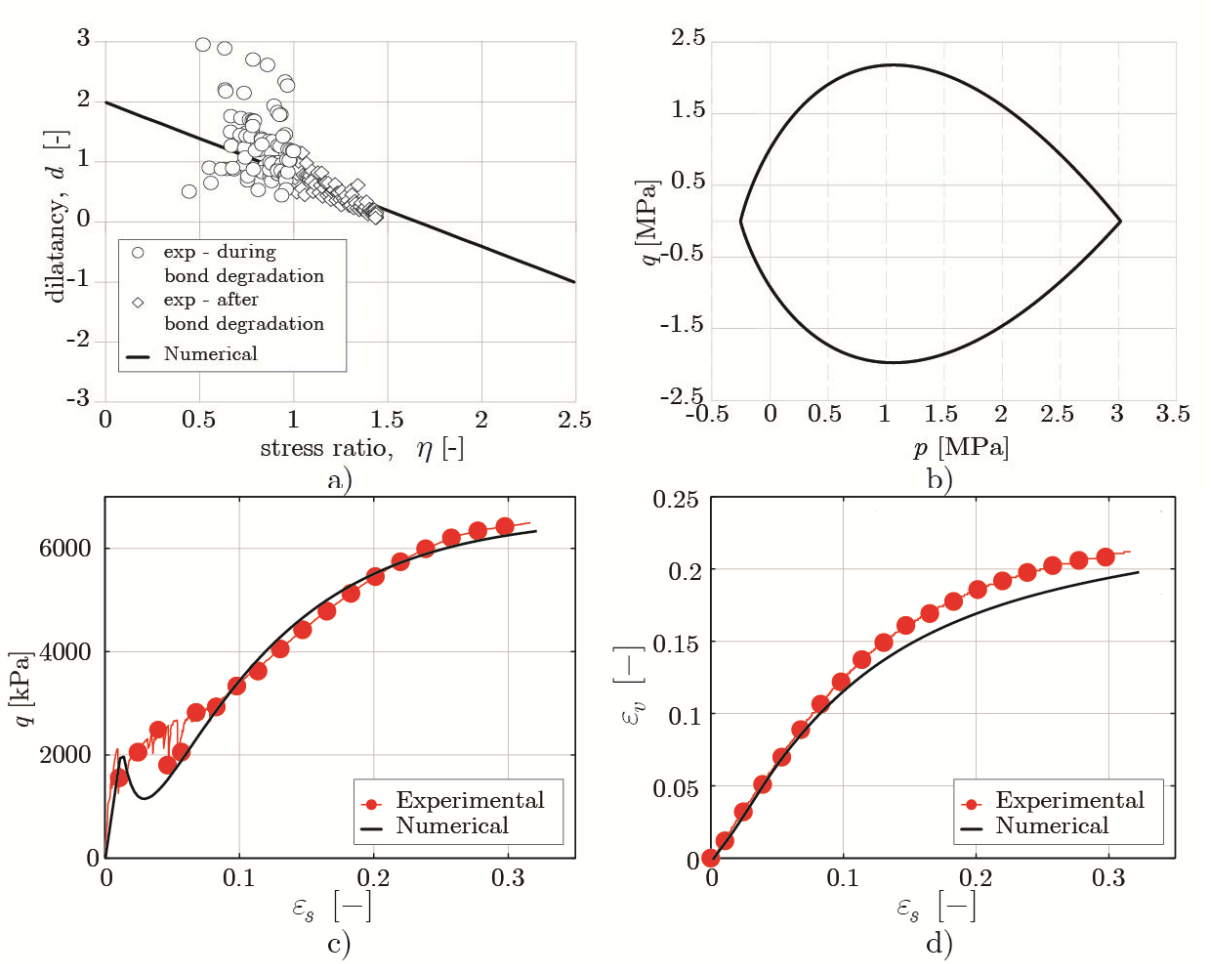

Fig. 9 Calibration of both the plastic potential and the mechanical degradation parameters: a) dilatancy versus stress ratio in drained triaxial compression test on a Gravina calcarenite (sample under a cell pressure of 2000 kPa), b) shape of the calibrated plastic potential, c,d) comparison between numerical simulations and experimental data for the Gravina calcarenite relative to a standard drained triaxial compression test with a confinement cell pressure of 2000 kPa.

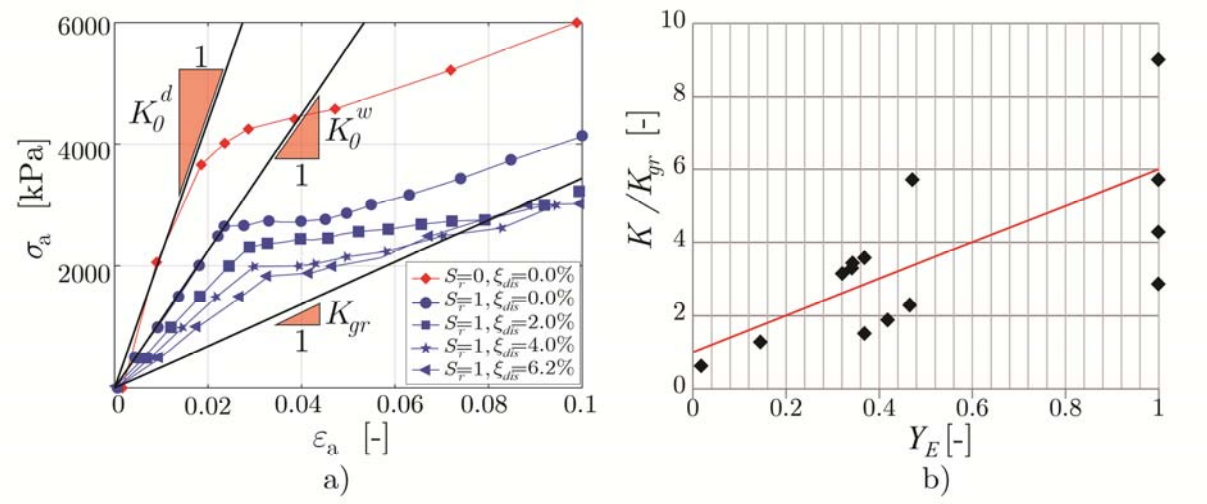

Fig. 10 Calibration of parameter δ_b: a) Oedometric compression test results on samples characterized by different values of ξ_{dis} corresponding to different values of Y_E, b) interpolating linear function describing the relationship between Y_E and K/K_{gr}.

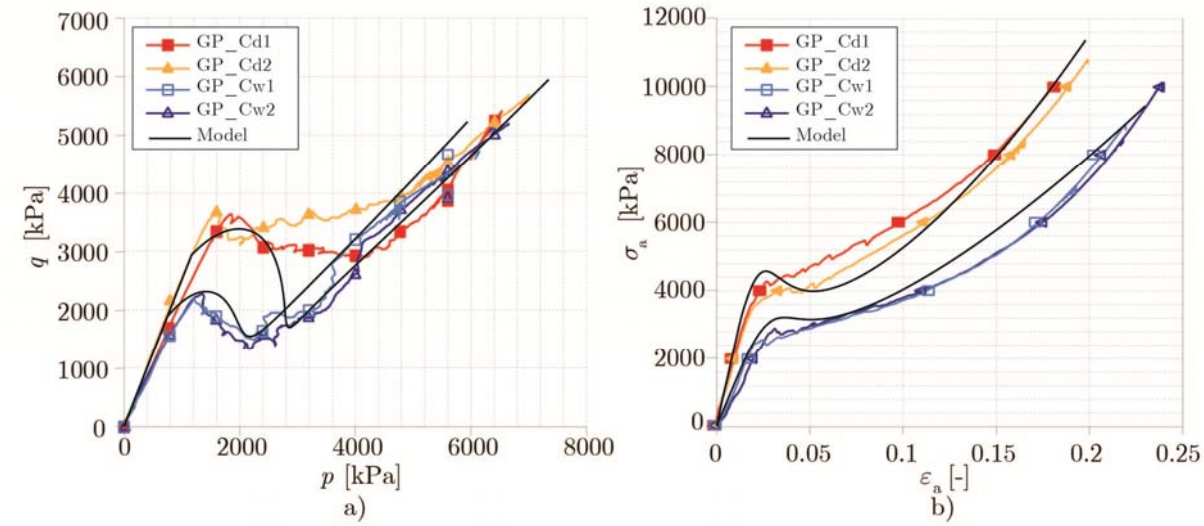

Fig. 11 Oedometric compression of calcarenite in dry and saturated conditions. a) stress path in deviatoric plane, b) vertical stress-strain relationship.

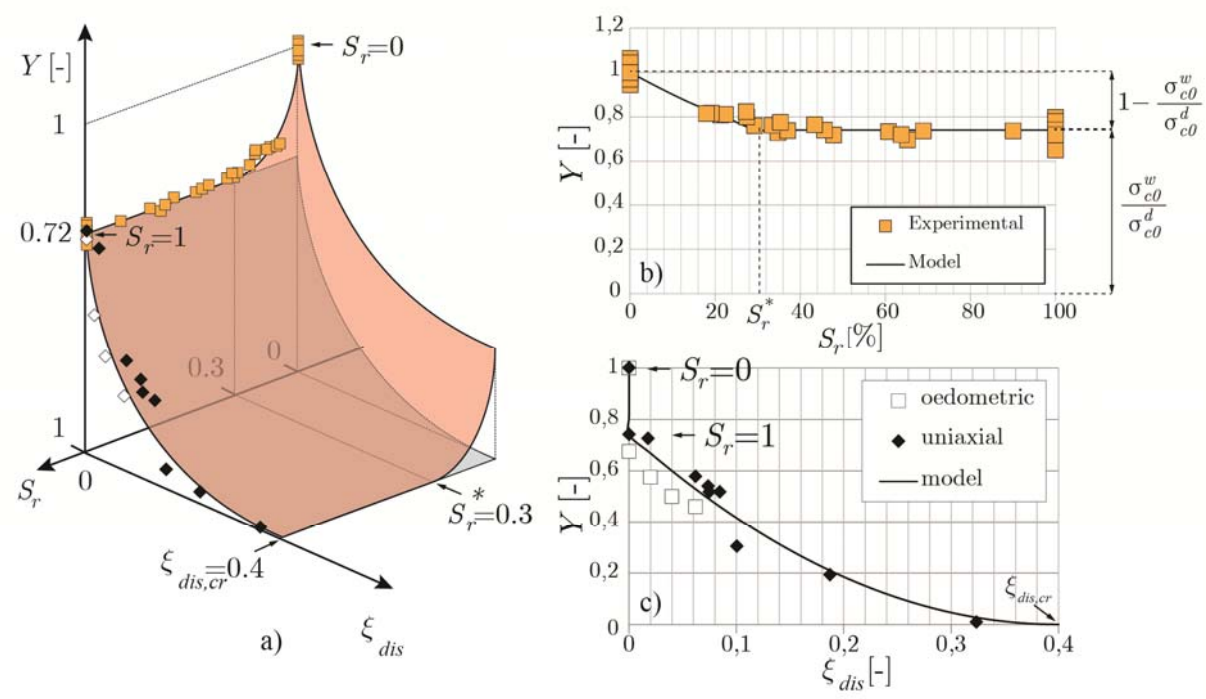

Fig. 12 Validation of the weathering function $Y(\xi_{dis}, S_r)$: a) 3D view of the weathering function and its comparison with experimental data from Ciantia et al 2014; weathering function with respect to b) degree of saturation and c) normalised accumulated dissolved mass.

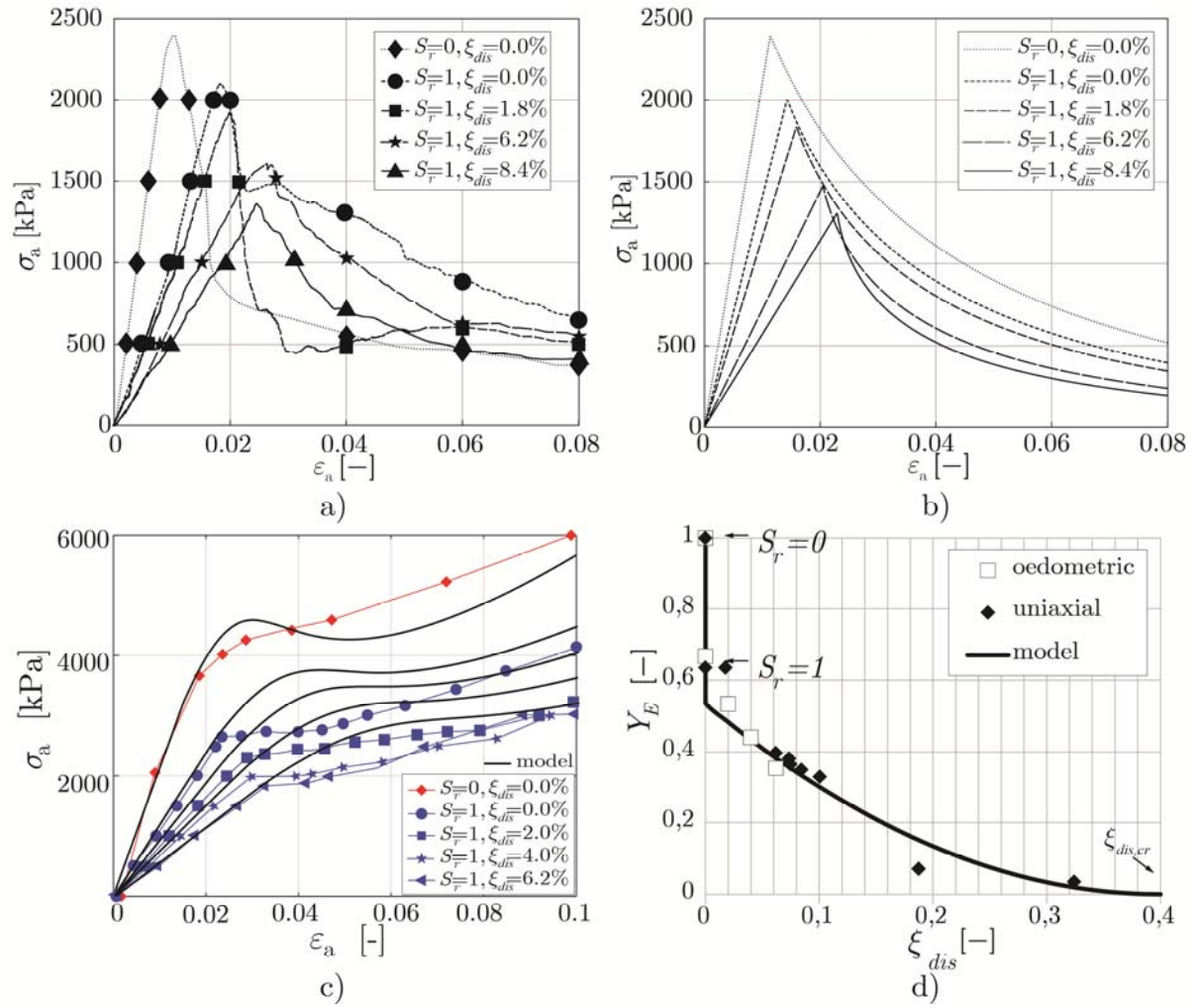

Fig. 13 a) Experimental results of uniaxial compression tests performed on Gravina Calcarenite at different levels of weathering (data from Ciantia et al 2014), b) numerical simulation of the latter uniaxial compression tests, c) comparison of numerical results and experimental data relative to oedometric compression tests performed on Gravina Calcarenite at different levels of weathering d) validation of stiffness weathering function $Y_E(\xi_{dis}, S_r)$.

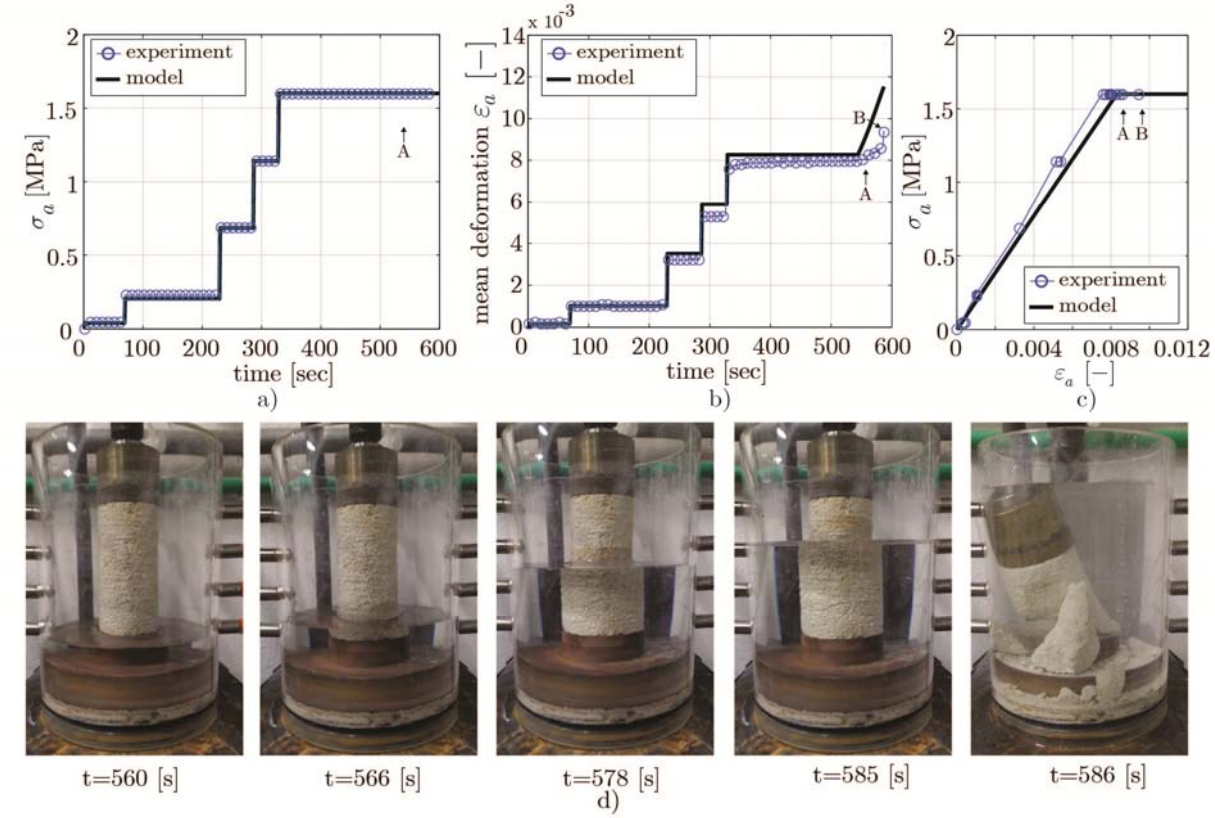

Fig. 14 Saturation induced failure of a small scale dry pillar: a) vertical stress versus time b) axial average deformation versus time, c) stress average-strain plot and d) sequence of photographs testifying the saturation phase.

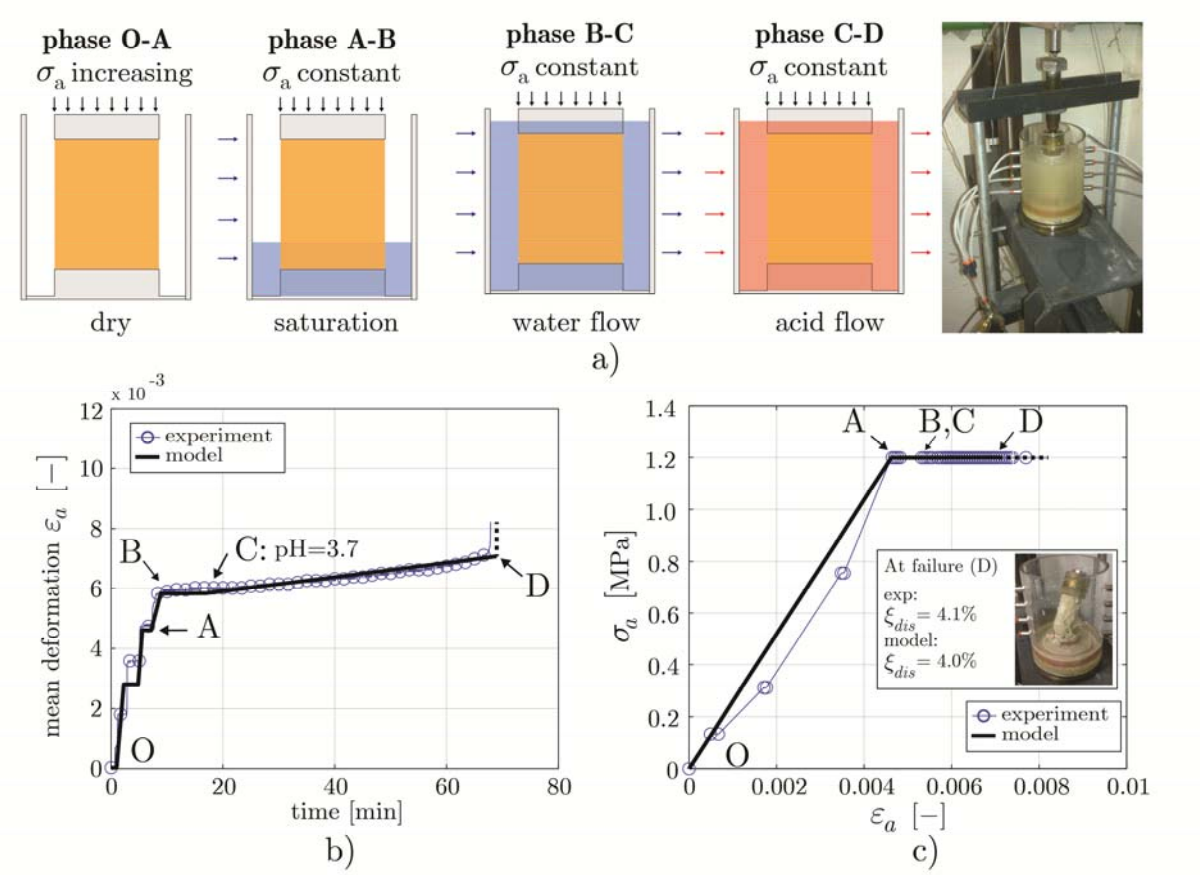

Fig. 15. Acid induced failure of a small scale pillar: a) test phases and picture of the experimental set up, b) stress path in the *p : q* plane, c) axial and radial strains versus time and d) stress strain response.

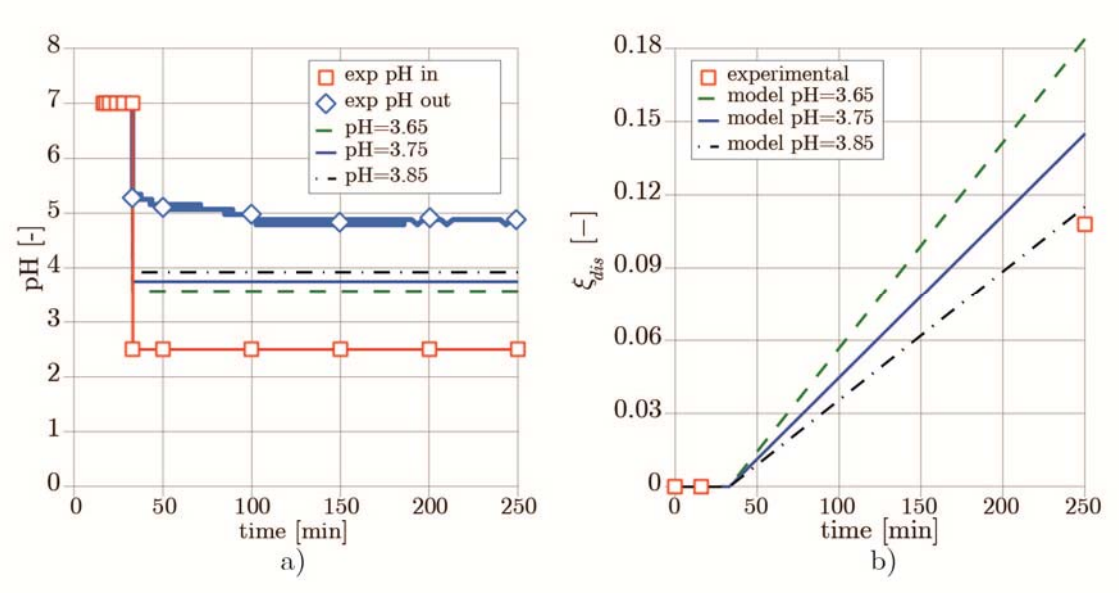

Fig. 16 Acid accelerated weathering under oedometric conditions: a) pH history imposed; b) comparison between measured and simulated ξ_{diss} as a function of time

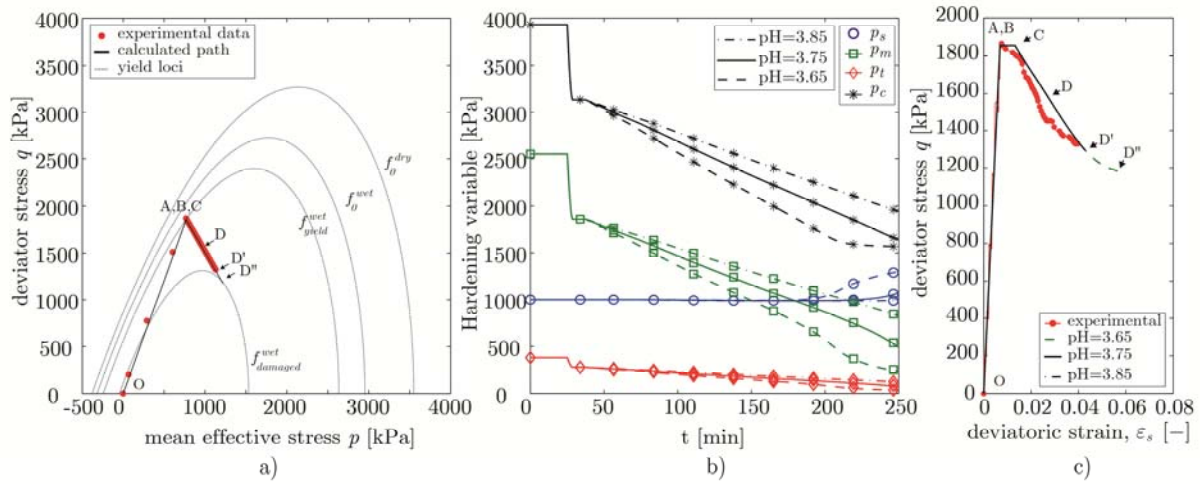

Fig. 17 Acid accelerated weathering under oedometric conditions: a) Experimental and theoretical stress path in the triaxial plane, b) evolution of internal variables controlling the size of the yield locus with time and c) deviatoric stress q versus deviatoric strains ε_s

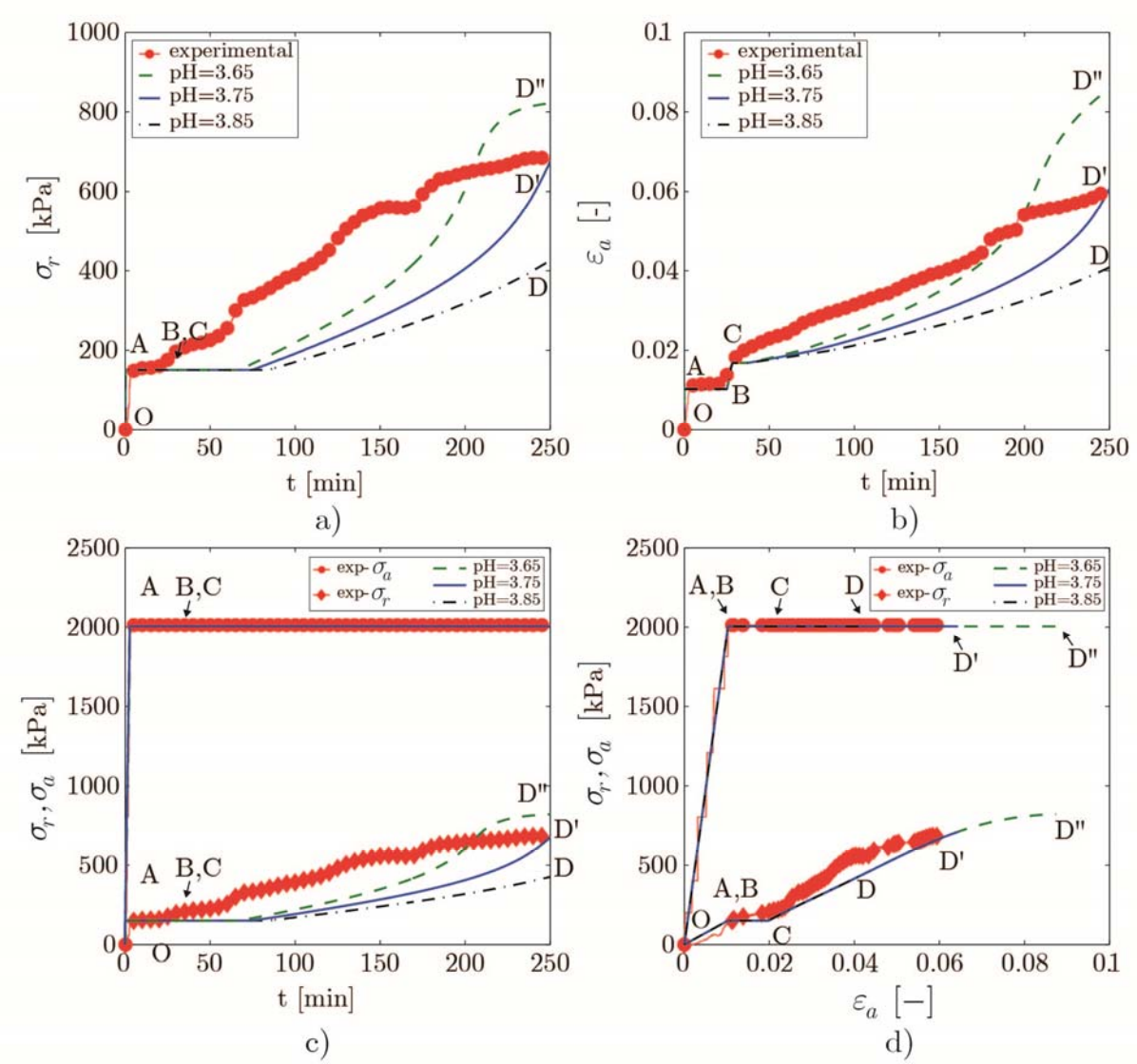

Fig. 18 Acid accelerated weathering under oedometric conditions: a) effective radial stress σ_r vs. time; b) Axial strain ε_a vs. time, (c), (d) radial σ_r and axial stress σ_a vs. time and vs. axial strain ε_a respectively.

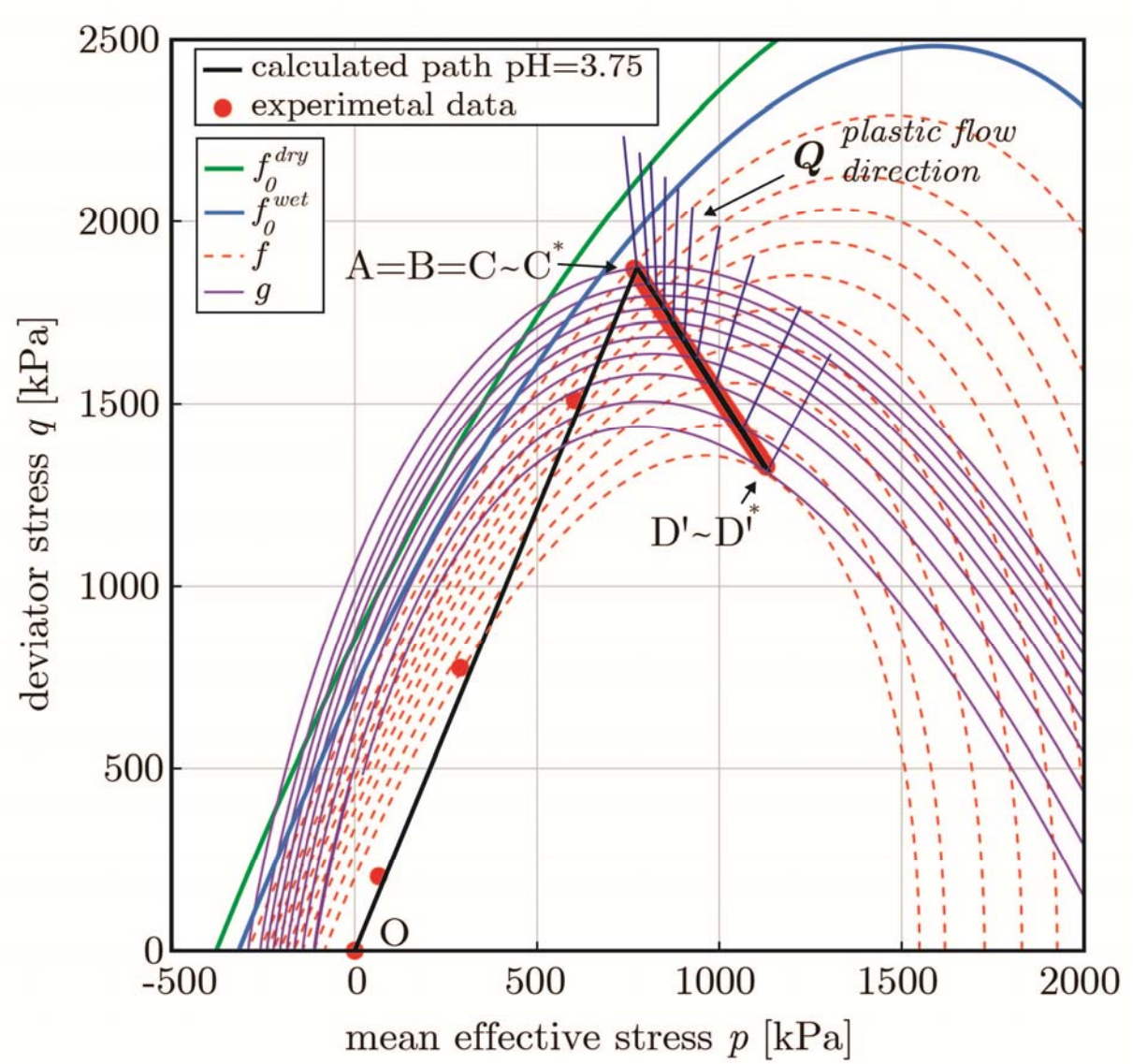

Fig. 19 Acid accelerated weathering under oedometric conditions: Stress path, evolution of the yield locus, plastic potential and plastic flow direction in the triaxial plane

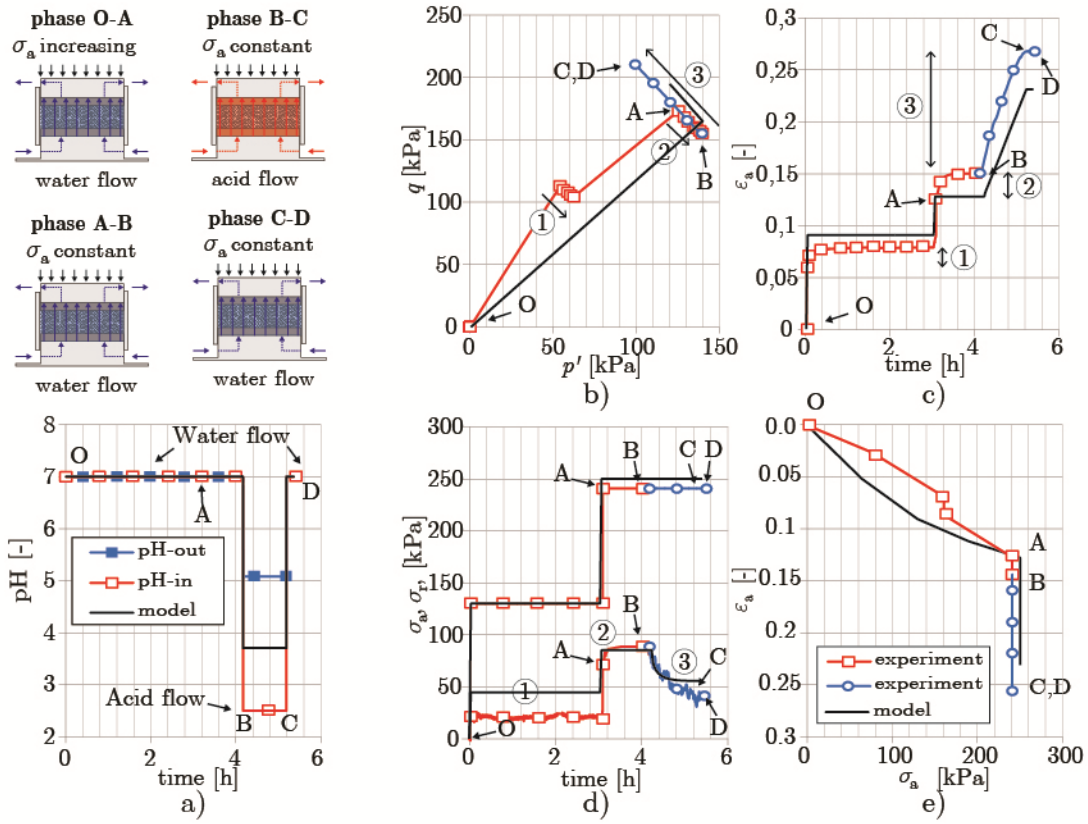

Fig. 20 Acid accelerated weathering of unbonded calcarenite under oedometric conditions: a) test phases and in-out pH measurements, b) stress path in the *p : q* plane, c) evolution of deformations with time, d) axial and radial stresses with respect to time, e) axial stress-strain curves.

10 Appendix A:

The damage variable D is formulated by using the isotropic damage introduced by Kachanov (1958) and applying the same multiscale approach adopted for the bond strength. Analogously to what done for the material strength (eq. (8)), the material stiffness can be written as:

$$\begin{cases} E = \mathrm{X}\bar{E}_0^d\left(1-\bar{D}\right) \\ E = E_0^d\left(1-D\right) \end{cases} \tag{50}$$

where E is the Young modulus, E_0^d is the Young modulus in the dry initial condition, X is an upscaling constant and D is the scalar damage variable. $\bar{E}_0^d$ and $\bar{D}$ represent the Young modulus in dry initial conditions and damage defined at the micro (bond) scale, respectively. Formulating damage at the micro-scale as:

$$\bar{D} = \frac{\Delta A}{A_0} = \frac{A_0 - n_{dia}\pi\left(r_{0,dia} - d\right)^2 + n_{dep}\pi\left(r_{0,dep} - d_{dep}\right)^2}{A_0} \tag{51}$$

where A_0 is the initial total bond area. By defining:

$$\begin{cases} \bar{Y}_E = \left(1-\bar{D}\right) \\ Y_E = \left(1-D\right) \end{cases} \tag{52}$$

the micro-scale and macro-scale stiffness weathering functions respectively, following the same approach used to determine the macro-scale weathering function it is possible to obtain:

$$\begin{cases} \bar{Y}_E = \left(1-\bar{D}\right) = \frac{r_{0,dia}^2 n_{dia}}{A_0}\left(1+\frac{\xi_{dis}^2}{\xi_{dis,cr}^2}-\frac{2\xi_{dis}}{\xi_{dis,cr}}\right)+\frac{r_{0,sus}^2 n_{dep}}{A_0}\left(1+\xi_{sus}^2-2\xi_{sus}\right) \\ Y_E = \left(1-D\right) = \frac{E_0^w}{E_0^d}\left(1-\frac{2\xi_{dis}}{\xi_{dis,cr}}+\frac{\xi_{dis}^2}{\xi_{dis,cr}^2}\right)+\frac{E_0^d-E_0^w}{E_0^d}\left(1-2\xi_{sus}+\xi_{sus}^2\right) \end{cases} \tag{53}$$

for $\xi_{dis} \le \xi_{dis,cr}$ (bonded material) and

$$\begin{cases} \overline{Y}_E = \left(1-\overline{D}\right) = \frac{r_{0,sus}^2 n_{sus}}{A_0}\left(1+\xi_{sus}^2 - 2\xi_{sus}\right) \\ Y_E = \left(1-D\right) = \frac{E_0^d - E_0^w}{E_0^d}\left(1-2\xi_{sus}+\xi_{sus}^2\right) \end{cases} \tag{54}$$

for $\xi_{dis} > \xi_{dis,cr}$ (unbonded material). Analogously to the weathering function in eq. (21), ξ_{sus} is related to the degree of saturation. Thus, the stiffness weathering function results:

$$Y_E = Y_{E,dis} + Y_{E,sus} \tag{55}$$

where

$$Y_{E,dis} = \begin{cases} \frac{E_0^w}{E_0^d}\left(1-\frac{\xi_{dis}}{\xi_{dis,cr}}\right)^2 & \xi_{dis} \le \xi_{dis,cr} \\ 0 & \xi_{dis} > \xi_{dis,cr} \end{cases} \tag{56}$$

and

$$Y_{E,sus} = \begin{cases} \frac{E_0^d - E_0^w}{E_0^d}\left(1-\frac{S_r}{S_r^*}\right)^2 & S_r \le S_r^* \\ 0 & S_r > S_r^* \end{cases} \tag{57}$$

for $\xi_{dis} > \xi_{dis,cr}$ (granular material). In conclusion eq. (29) can be recast as

$$\boldsymbol{D}^e\left(\varepsilon^e, Y\right) = \boldsymbol{D}^e\left(\varepsilon^e\right)\left(1+\delta_b Y_E\right) \tag{58}$$

11 Appendix B:

According to eqs.(38), (33) and (5), the evolution in time of the state variables ($\boldsymbol{\sigma}$, $\boldsymbol{q}$) is governed by the following system of ordinary differential equations:

$$\dot{\boldsymbol{\sigma}} = \boldsymbol{D}^e \left[\dot{\boldsymbol{\varepsilon}} - \dot{\Lambda} \frac{\partial g}{\partial \boldsymbol{\sigma}} - \dot{\boldsymbol{\varepsilon}}^c \right] + \boldsymbol{D}_M \dot{Y}_E \tag{59}$$

$$\dot{\boldsymbol{q}} = \dot{\Lambda} \boldsymbol{h}\left(\boldsymbol{\sigma}, \boldsymbol{q}, Y\right) + \boldsymbol{\eta}\left(\boldsymbol{\sigma}, \boldsymbol{q}, Y\right) \dot{Y} \tag{60}$$

subject to the algebraic constraint posed by the Kuhn–Tucker complementarity conditions (Nova, 2012). For a plastic state, in which $f = 0$, the constraint $\mathbb{E}_\sigma := \left\{ \left(\boldsymbol{\sigma}, \boldsymbol{q}\right) \middle| \, f\left(\boldsymbol{\sigma}, \boldsymbol{q}\right) \le 0 \right\}$ implies that (see, e.g., Simo and Hughes, 1997):

$$\dot{f} = \frac{\partial f}{\partial \boldsymbol{\sigma}} \cdot \dot{\boldsymbol{\sigma}} + \frac{\partial f}{\partial \boldsymbol{q}} \cdot \dot{\boldsymbol{q}} \le 0 \tag{61}$$

According to the consistency condition, if $\dot{f} < 0$ then $\dot{\Lambda} = 0$ and the process is elastic (*elastic unloading* from a plastic state). On the other hand, if $\dot{f} = 0$ then plastic strains can occur ($\dot{\Lambda} > 0$, *plastic loading*). Taking into account the constitutive equation (59) and the hardening law(60), if plastic loading occurs, then:

$$\begin{aligned} &\frac{\partial f}{\partial \boldsymbol{\sigma}} \cdot \boldsymbol{D}^e \dot{\boldsymbol{\varepsilon}} + \frac{\partial f}{\partial \boldsymbol{q}} \cdot \boldsymbol{\eta} \dot{Y} + \frac{\partial f}{\partial \boldsymbol{\sigma}} \cdot \boldsymbol{D}_M \dot{Y}_E - \frac{\partial f}{\partial \boldsymbol{\sigma}} \cdot \boldsymbol{D}^e \dot{\boldsymbol{\varepsilon}}^c + \\ &- \dot{\Lambda} \left(\frac{\partial f}{\partial \boldsymbol{\sigma}} \cdot \boldsymbol{D}^e \frac{\partial g}{\partial \boldsymbol{\sigma}} - \frac{\partial f}{\partial \boldsymbol{q}} \cdot \boldsymbol{h} \right) = 0 \end{aligned} \tag{62}$$

Assuming that, for all admissible states ($\boldsymbol{\sigma}$, $\boldsymbol{q}$), the yield condition, the flow rule and the hardening law are such that the inequality:

$$K_p := \frac{\partial f}{\partial \boldsymbol{\sigma}} \cdot \boldsymbol{D}^e \frac{\partial g}{\partial \boldsymbol{\sigma}} - \frac{\partial f}{\partial \boldsymbol{q}} \cdot \boldsymbol{h} > 0 \tag{63}$$

is *always* satisfied, then eq. (62) provides the following expression for the plastic multiplier:

$$\dot{\Lambda} = \frac{1}{K_p} \left\langle \frac{\partial f}{\partial \boldsymbol{\sigma}} \cdot \boldsymbol{D}^e \dot{\boldsymbol{\varepsilon}} + \frac{\partial f}{\partial \boldsymbol{q}} \cdot \boldsymbol{\eta} \dot{Y} + \frac{\partial f}{\partial \boldsymbol{\sigma}} \cdot \boldsymbol{D}_M \dot{Y}_E - \frac{\partial f}{\partial \boldsymbol{\sigma}} \cdot \boldsymbol{D}^e \dot{\boldsymbol{\varepsilon}}^c \right\rangle \tag{64}$$

in which $\langle x \rangle := \left(x + |x| \right) / 2$ is the ramp function.

Substituting the above expression for the plastic multiplier in eqs. (59) and (60), the time rates of $\boldsymbol{\sigma}$ and $\boldsymbol{q}$ can be expressed as a function of the corresponding rates of the total strain $\boldsymbol{\varepsilon}$ and the weathering function Y as follows:

$$\dot{\boldsymbol{\sigma}} = \boldsymbol{D} \dot{\boldsymbol{\varepsilon}} + \boldsymbol{D}_Y \dot{Y} + \boldsymbol{D}_{Y_E} \dot{Y}_E + \boldsymbol{D}_c \dot{\boldsymbol{\varepsilon}}^c \tag{65}$$

$$\dot{\boldsymbol{q}} = \boldsymbol{G} \dot{\boldsymbol{\varepsilon}} + \boldsymbol{G}_Y \dot{Y} + \boldsymbol{G}_{Y_E} \dot{Y}_E + \boldsymbol{G}_c \dot{\boldsymbol{\varepsilon}}^c \tag{66}$$

where:

$$\boldsymbol{D} := \boldsymbol{D}^e - \frac{1}{K_p} \left(\boldsymbol{D}^e \frac{\partial g}{\partial \boldsymbol{\sigma}} \right) \otimes \left(\frac{\partial f}{\partial \boldsymbol{\sigma}} \boldsymbol{D}^e \right) \tag{67}$$

$$\boldsymbol{D}_Y := -\frac{1}{K_p} \left(\frac{\partial f}{\partial \boldsymbol{q}} \cdot \boldsymbol{\eta} \right) \boldsymbol{D}^e \frac{\partial g}{\partial \boldsymbol{\sigma}} \tag{68}$$

$$\boldsymbol{D}_{Y_E} := -\frac{1}{K_p} \left(\frac{\partial f}{\partial \boldsymbol{\sigma}} \cdot \boldsymbol{D}_M \right) \boldsymbol{D}^e \frac{\partial g}{\partial \boldsymbol{\sigma}} + \boldsymbol{D}_M \tag{69}$$

$$\boldsymbol{D}_c \coloneqq -\boldsymbol{D}^e + \frac{1}{K_p}\left(\boldsymbol{D}^e \frac{\partial g}{\partial \boldsymbol{\sigma}}\right) \otimes \left(\frac{\partial f}{\partial \boldsymbol{\sigma}} \boldsymbol{D}^e\right) \tag{70}$$

$$\boldsymbol{G} \coloneqq \frac{1}{K_p} \boldsymbol{h} \otimes \left(\frac{\partial f}{\partial \boldsymbol{\sigma}} \boldsymbol{D}^e\right) \tag{71}$$

$$\boldsymbol{G}_Y \coloneqq \frac{1}{K_p}\left(\frac{\partial f}{\partial \boldsymbol{q}} \cdot \boldsymbol{\eta}\right)\boldsymbol{h} + \boldsymbol{\eta} \tag{72}$$

$$\boldsymbol{G}_{Y_E} \coloneqq \frac{1}{K_p}\left(\frac{\partial f}{\partial \boldsymbol{\sigma}} \cdot \boldsymbol{D}_M\right)\boldsymbol{h} \tag{73}$$

$$\boldsymbol{G}_c \coloneqq -\frac{1}{K_p} \boldsymbol{h} \otimes \left(\frac{\partial f}{\partial \boldsymbol{\sigma}} \boldsymbol{D}^e\right) \tag{74}$$

for plastic loading processes ($\dot{\Lambda} > 0$), and:

$$\boldsymbol{D} \coloneqq \boldsymbol{D}^e \quad ; \quad \boldsymbol{G} \coloneqq \boldsymbol{0} \tag{75}$$

$$\boldsymbol{D}_Y \coloneqq \boldsymbol{0} \quad ; \quad \boldsymbol{G}_Y \coloneqq \boldsymbol{\eta} \tag{76}$$

$$\boldsymbol{D}_{Y_E} \coloneqq \boldsymbol{D}_M \quad ; \quad \boldsymbol{G}_{Y_E} \coloneqq \boldsymbol{0} \tag{77}$$

$$\boldsymbol{D}_c \coloneqq -\boldsymbol{D}^e \quad ; \quad \boldsymbol{G}_c \coloneqq \boldsymbol{0} \tag{78}$$

the second and fourth order tensors in eq. (47) hence result:

$$D_{ijhk}^{ep} = \boldsymbol{D} \tag{79}$$

$$D_{ij}^{LTD} = \boldsymbol{D}_Y \Xi \tag{80}$$

$$D_{ij}^{DAMAGE-dia} = \boldsymbol{D}_{Y_E} \Xi_E \tag{81}$$

$$D_{ij}^{GDP} = \boldsymbol{D}_c \boldsymbol{I}_3 C \tag{82}$$

$$D_{ij}^{STD} = \boldsymbol{D}_Y \Sigma \tag{83}$$

$$D_{ij}^{DAMAGE-dep} = \boldsymbol{D}_{Y_E} \Sigma_E \tag{84}$$